

CONFOCAL FABRY-PEROT INTERFEROMETER BASED
HIGH SPECTRAL RESOLUTION LIDAR

by

David Swick Hoffman

A dissertation submitted in partial fulfillment
of the requirements for the degree

of

Doctor of Philosophy

in

Engineering

MONTANA STATE UNIVERSITY
Bozeman, Montana

September, 2012

© COPYRIGHT

by

David Swick Hoffman

2012

All Rights Reserved

APPROVAL

of a dissertation submitted by

David Swick Hoffman

This dissertation has been read by each member of the dissertation committee and has been found to be satisfactory regarding content, English usage, format, citations, bibliographic style, and consistency, and is ready for submission to The Graduate School.

Dr. Kevin S. Repasky

Approved for the Department of Electrical and Computer Engineering

Dr. Robert C. Maher

Approved for The Graduate School

Dr. Ronald W. Larsen

STATEMENT OF PERMISSION TO USE

In presenting this dissertation in partial fulfillment of the requirements for a doctoral degree at Montana State University, I agree that the Library shall make it available to borrowers under rules of the Library. I further agree that copying of this dissertation is allowable only for scholarly purposes, consistent with “fair use” as prescribed in the U.S. Copyright Law. Requests for extensive copying or reproduction of this dissertation should be referred to ProQuest Information and Learning, 300 North Zeeb Road, Ann Arbor, Michigan 48106, to whom I have granted “the exclusive right to reproduce and distribute my dissertation in and from microform along with the non-exclusive right to reproduce and distribute my abstract in any format in whole or in part.”

David Swick Hoffman

September, 2012

TABLE OF CONTENTS

1. INTRODUCTION	1
Earth's Atmosphere	1
Atmospheric Aerosols	3
Lidar	4
High Spectral Resolution Lidar	6
2. HSRL INSTRUMENT.....	11
HSRL Instrument Layout	11
Confocal Fabry-Perot Interferometer	15
CFP Design	18
Locking	24
Data Acquisition.....	33
3. THEORY AND DATA ANALYSIS	35
4. DATA	42
5. ERROR ANALYSIS.....	68
Detector Signal to Noise Calculations.....	68
Quantization Error.....	76
Numerical Differentiation Error.....	78
Error Impact Summary	79
6. CONCLUDING REMARKS	80
REFERENCES CITED.....	82
APPENDIX A: Matlab Code.....	86

LIST OF TABLES

Table	LIST OF TABLES	Page
1	Transmitter and Receiver Parameters.	14

LIST OF FIGURES

Figure		Page
1	A diagram of the layers in the middle and lower atmosphere. The Planetary Boundary Layer is of special interest since it contains the highest concentration of atmospheric aerosols.....	2
2	A basic lidar system diagram. Light is emitted from a transmitter, travels through the atmosphere and is scattered by a target. Some of the scattered light is observed by a receiver. The pulse of light emitted from the receiver will take r/c time to travel to a target at range r and another r/c for light scattered by the target to reach the receiver, where c is the speed at which light travels through the atmosphere. It will therefor take $2r/c$ time for the total round trip of the light. The range to the target can then be calculated by $r = \frac{total\ time}{2}c$	5
3	A gas absorption feature (Iodine is frequently used in HSRL instruments) overlays a plot of the spectral profile of a lidar return on the left. The central aerosol peak is blocked by the gas, leaving the molecular "wings" seen in the right-hand plot.....	9
4	A flow diagram detailing the operation of the HSRL instrument.....	12
5	A schematic of the HSRL instrument.....	13
6	A plot of CFP transmission vs incident light frequency for a cavity length of 1 cm.	17
7	A plot of CFP transmission compared to the spectral distribution of light backscattered by the atmosphere. The CFP transmitted most of the central aerosol peak, while reflected most of the molecular "wings.".....	18
8	Normalized theoretical CFP transmission for mirror reflectivities .88 - .96.....	20
9	The mechanical layout of the CFP used in the HSRL instrument.	21
10	A photo of the CFP used in the HSRL instrument.	22
11	The configuration used to test the optimal positioning of the cavity to filter multimode light from a 200 μm fiber.	23
12	A plot of CFP finesse vs distance Z between lens 2 (see figure 11) and the CFP. The angular content of the incident light is a function of distance Z , and beam diameter at lens 2 D	25

LIST OF FIGURES – CONTINUED

Figure		Page
13	A plot of CFP transmission and reflectivity while the cavity length is scanned via piezo-electric transducer. The top plot is CFP reflectivity and transmission at 532 nm, and the bottom plot is 1064 nm transmission. The small side-lobe in the 1064 nm signal is present because the 1064 nm beam has been aligned for perfect resonance overlap with the 532 nm signal, rather than high finesse.	26
14	A flow diagram depicting the locking of the CFP to the 1064 nm seed laser. The dashed lines represent an optical signal traveling from the AOM through the CFP to the 1064 nm detector, while the solid lines represent electrical signals.	27
15	Cavity transmission, AOM drive signal (proportional to incident light wavelength shift) and resulting error signal for three different cavity lengths. The column on the left corresponds to an oversized cavity, the column on the right corresponds to an undersized cavity and the center column corresponds to the desired cavity length. Note that these signals are plotted over $\frac{1}{2}$ period of the reference sinusoid that drives the AOM. The other $\frac{1}{2}$ period is a reflection of these plots and has been omitted for simplicity.	29
16	A photo of the locking optical train. The green lines represent the green science channel light, while the red lines represent the 1064 nm light from the seed laser used to lock the cavity. The green channel detectors have been replaced with PMTs for use in data collection.	30
17	A circuit which actively maintains the mirror spacing within the CFP such that the CFP remains resonant at the 1064 nm seed laser wavelength.	32
18	A flow diagram of the data acquisition process.	34
19	Range resolved, modeled molecular backscatter coefficient.	38
20	A plot of the attenuated molecular backscatter as a function of range is shown as the solid black line. The modeled molecular backscatter is shown as the dotted blue line in this figure.	44
21	A plot of the attenuated aerosol backscatter as a function of range. The aerosols are mostly confined below the planetary boundary layer at approximately 1.1 km.	45

LIST OF FIGURES – CONTINUED

Figure		Page
22	The aerosol backscatter as a function of range calculated by scaling the modeled molecular backscatter by the ratio of the measured aerosol and molecular return signals shown in figures 8 and 9.	46
23	The lidar ratio as a function of range retrieved from the aerosol and molecular signals shown in figures 8 and 9 is plotted as the solid line. The lidar ratio is plotted from 600 m where the HSRL comes into full overlap to the planetary boundary layer at 1.1 km. The vertical line represents the column averaged lidar ratio calculated from the inverted AERONET data. The lidar data used to calculate the SA were collected at 17:48 UTC, while the AERONET data used in the inversion was collected at 18:37 UTC.	47
24	A plot of the attenuated molecular backscatter as a function of range is shown as the solid black line. The modeled molecular backscatter is shown as the dotted blue line in this figure.	49
25	A plot of the attenuated aerosol backscatter as a function of range.	50
26	A plot of the retrieved S_A . The mean S_A within the planetary boundary layer is represented by the dotted line.	51
27	A plot of the aerosol extinction as a function of range. The aerosols are mostly contained below the planetary boundary layer at approximately 1.6 km with an aerosol layer forming near the boundary layer.	52
28	A plot of the aerosol attenuated backscatter as a function of range.	53
29	A plot of the molecular attenuated backscatter as a function of range.	54
30	A plot of the aerosol extinction to backscatter as a function of range.	55
31	A plot of the aerosol attenuated backscatter as a function of range.	56
32	A plot of the aerosol extinction to backscatter ratio as a function of range.	57
33	A plot of the aerosol extinction to backscatter ratio as a function of range.	58
34	A plot of the aerosol extinction to backscatter ratio as a function of range.	59

LIST OF FIGURES – CONTINUED

Figure		Page
35	A plot of the aerosol extinction to backscatter ratio as a function of range.	60
36	A plot of the retrieved aerosol lidar return for May 7 th	62
37	A plot of the retrieved molecular lidar return for May 7 th . The blue line represents a modeled molecular return with no aerosol contribution.	63
38	A plot of the retrieved aerosol backscatter coefficient as a function of range for May 7 th	64
39	A plot of the aerosol extinction to backscatter ratio as a function of range for May 7 th	65
40	A time-series plot of the retrieved aerosol return for May 7 th	66
41	A time-series plot of the aerosol extinction to backscatter ratio as a function of range for May 7 th	67
42	The worst case effects of detector error on S_A retrieval.	69
43	A modeled time-series of lidar returns observed at a single range bin in the frequency domain. The single low frequency spike represents the high-frequency limit expected in real data.	70
44	The frequency response of a 10-point averaging filter.	71
45	A modeled time-series of lidar returns observed at a single range bin in the frequency domain, after a filter has been applied to reduce the noise-content.	72
46	A modeled lidar return with a noise level consistent with that produced by the PMTs in the HSRL.	73
47	The result of applying a thirty-point averaging filter to the modeled data shown in figure 46.	74
48	The frequency response of a thirty-point averaging filter.	75

LIST OF FIGURES – CONTINUED

Figure		Page
49	Quantization error is the difference between the actual signal and its quantized value; quantization occurs when the signal is digitized using an A/D converter. In this figure, the red vertical lines represent the quantization error, the blue horizontal lines along the left side mark the quantization levels and the blue vertical lines along the bottom mark the sample points where the original signal (the green line) is sampled and subsequently quantized.....	77
50	Quantization can be modeled as adding the error term $e[n]$ to the sampled signal, where $e[n]$ is uniformly distributed random noise.....	77
51	Percent error resulting from using numerical differentiation in the data analysis software. Note that at 200 MHz (the sample rate of the two-wavelength lidar instrument), the error is approximately $2.5 \times 10^{-4}\%$	78

ABSTRACT

A high spectral resolution lidar (HSRL), which has been developed at Montana State University, utilizes a confocal Fabry-Perot interferometer (CFP) to separate aerosol and molecular lidar returns for the purpose of atmospheric aerosol observation. The CFP is actively frequency locked to the laser-transmitter via a novel frequency modulation based technique. 532 nm second harmonic light from a frequency doubled Nd:YAG injectionseeded, pulsed laser is directed vertically into the atmosphere. Light backscattered by the atmosphere is collected using a commercial Schmidt-Cassegrain telescope. The secondharmonic return signal is mode matched into a tunable CFP interferometer with a free spectral range of 7.5 GHz and a finesse of 50.7 (312) at 532 nm (1064 nm) placed in the optical receiver for spectrally filtering the molecular and aerosol return signals. The light transmitted through the CFP is used to monitor the aerosol return signal while the light reflected by the CFP is used to monitor the molecular return signal. Data collected with the HSRL are presented and inversion results are compared to those from a co-located solar radiometer, demonstrating the successful operation of the instrument. The HSRL presented in this dissertation provides an important means to study atmospheric aerosols, which are the largest source of uncertainty in current global climate models. Additionally, the novel frequency locking technique allows for the future development of multi-wavelength HSRL instruments, and the robustness of the frequency locked optical filter allows for the deployment of future air and space based HSRL instruments.

INTRODUCTION

This dissertation presents a high spectral resolution lidar (HSRL) instrument which has been constructed for the purpose of studying atmospheric aerosols. Atmospheric aerosol optical properties are of great interest to climate scientists and modelers because they play an important, but difficult to quantify, role in global climate and temperature. The HSRL instrument uses a novel confocal Fabry-Perot (CFP) interferometer to separate aerosol and molecular lidar returns. The CFP is portable to arbitrary wavelengths, unlike previously used molecular absorption filters, and is much simpler to use and more robust than previously used flat-plate interferometers. The CFP is frequency locked to a cw laser which is used to seed a pulsed, frequency-doubled Nd:YAG laser which illuminates the atmosphere. By locking at the fundamental 1064nm and filtering at 532 nm, no modulation or dithering occurs at the 532 nm wavelength, and no polarization optics are needed to keep the science and locking light separate. Initial data are presented, demonstrating successful data collection and aerosol optical property retrieval. The HSRL instrument presented in this dissertation utilizes novel filtering and locking techniques, and represents a step forward in HSRL technology by demonstrating the feasibility of constructing future HSRL instruments at multiple/arbitrary wavelengths.

Earth's Atmosphere

The atmosphere is composed of many layers based on temperature trends, and consists of various gases and particulate matter. Figure 1 shows the layers in the middle and lower atmosphere starting with the Planetary Boundary Layer (PBL) near the ground and extending through the Mesosphere. Most of the aerosol mass

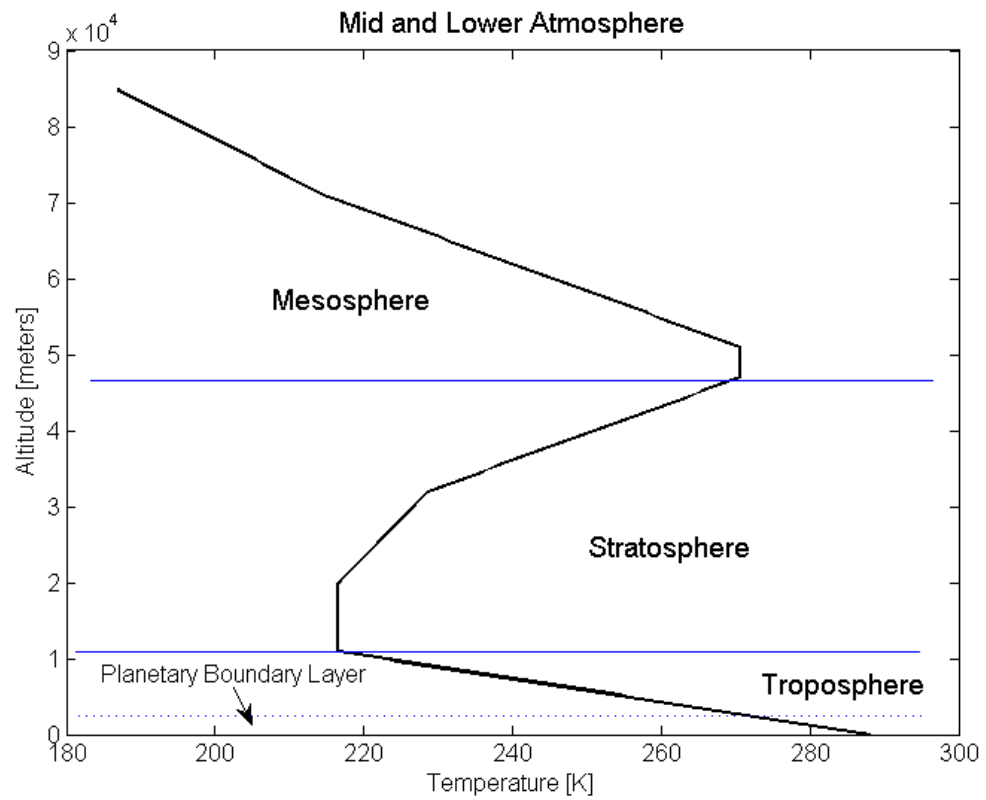


Figure 1: A diagram of the layers in the middle and lower atmosphere. The Planetary Boundary Layer is of special interest since it contains the highest concentration of atmospheric aerosols.

suspended in the atmosphere resides within the PBL, which is the atmospheric layer directly above the ground. This layer is generally very turbulent (due to surface features, friction, wind shear and thermal convection), and is strongly influenced by ground conditions. The PBL can be heated or cooled directly by the ground, and can also pick up aerosols from the ground, such as blowing dust, or smoke from fires. While most of these aerosols remain within the PBL, some can be transported into other layers of the atmosphere and travel long distances. Atmospheric aerosols can affect atmospheric chemistry, cloud formation, weather and climate.

Atmospheric Aerosols

Atmospheric aerosols are widely understood to play a significant role in the planetary radiation budget; however, there are still many unknowns surrounding the radiative forcing (the effect on the local radiation-energy budget) of aerosols (for more information on radiative forcing see [1, 2]). The direct and indirect forcing effects of aerosols each influence the global climate significantly and both need to be better understood in order to create accurate climate models [3, 1]. Direct radiative forcing is caused by the scattering and absorption of incoming solar radiation by atmospheric aerosols. The direct effects of aerosol absorption are strongly dependent on altitude and geographic location, meaning that ground sampling of aerosols often can provide misleading information about their overall radiative forcing [4, 1]. Absorbing aerosols in the upper atmosphere over dark surfaces such as large bodies of water produce a negative forcing, while the same aerosols positioned lower in the atmosphere, or over a lighter surface such as a snow-field will produce a positive forcing. Scattering aerosols generally produce a negative radiative forcing, estimated to be approximately $-1.9W/m^2$ [5, 1]. The complexity of the direct radiative forcing effects, compounded

by the short atmospheric lifetime of aerosols, clearly demonstrates the need for more study of aerosols and their radiative forcing.

Cloud-aerosol microphysical interactions make up the most significant aerosol radiative indirect effects [6, 2]. These interactions affect cloud formation, lifetime, albedo and other properties. For example, the interaction between airborne pollution from Asia and convective cloud formation above the Pacific Ocean has been shown to increase the intensity of Pacific storms [7]. The most significant aerosol indirect radiative forcing is caused by the effect of aerosols on cloud albedo [8]. As of the publication of the latest Intergovernmental Panel on Climate Change report, radiative forcing due to aerosol induced changes in cloud albedo varied widely from -0.22 to $-2.00[W/m^2]$ [1]. The effects of different aerosols on cloud albedo are highly dependent on both the concentration and the chemical properties of the aerosols in question [9]. The cloud albedo related indirect forcing effects of aerosols are a large source of uncertainty in global climate models [1].

Aerosol concentrations can change rapidly and their forcing effects are highly dependent on aerosol species, geographic location and altitude [7]. The radiative forcing of aerosols is one of the largest sources of error and uncertainty in current climate models [1]. New studies are needed to learn more about global aerosol distributions and radiative forcing. Such studies could improve the accuracy of future global climate models. It is therefore very important to develop new instrumentation for altitude-resolved study and tracking of atmospheric aerosols.

Lidar

Lidar (Light Detection and Ranging) involves illuminating a target (in this case the atmosphere) with light and observing the light that is scattered back in order to gain

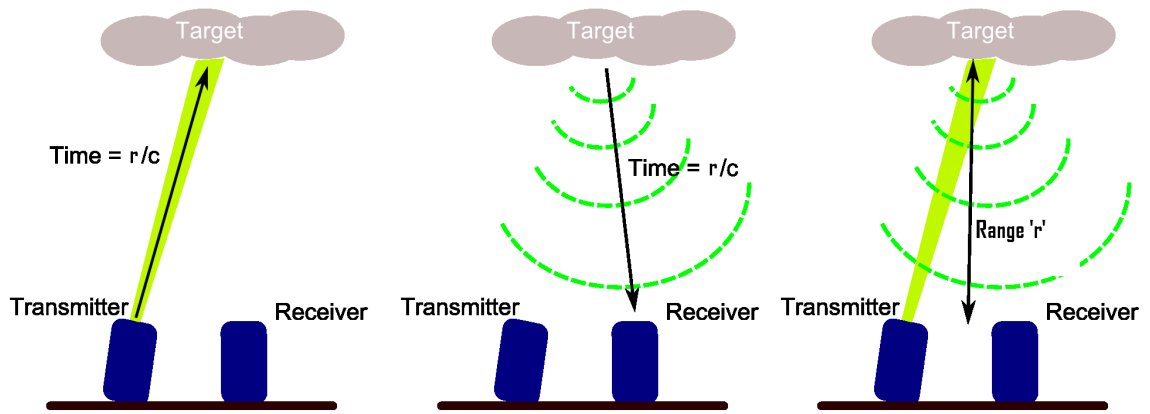


Figure 2: A basic lidar system diagram. Light is emitted from a transmitter, travels through the atmosphere and is scattered by a target. Some of the scattered light is observed by a receiver. The pulse of light emitted from the receiver will take r/c time to travel to a target at range r and another r/c for light scattered by the target to reach the receiver, where c is the speed at which light travels through the atmosphere. It will therefore take $2r/c$ time for the total round trip of the light. The range to the target can then be calculated by $r = \frac{\text{total time}}{2}c$.

information about that target [10]. Depending on the nature of the lidar instrument being used, different features of the target of interest can be observed either directly or indirectly. For example, the distance to an object can be measured by observing the time taken by light to travel to the object, be reflected or scattered, and travel back to the lidar instrument as illustrated in fig. 2. Lasers are a commonly used light source in lidar instruments because they enable spatially, temporally and spectrally precise illumination of a desired target. By observing the temporal and spectral distribution as well as the intensity of the light that is backscattered, inferences can be made about physical and chemical properties of the target.

The first lidar instruments appeared in the 1930's, utilizing a camera offset from a vertically pointing spot-light to record scattering intensity [11]. This technique was soon improved through the use of a pulsed light source and co-located detector which

used pulse time-of-flight to make range resolved scattering measurements. The advent of the laser in 1960 greatly improved the effectiveness of lidar instruments, and by 1963, a pulsed ruby laser had been used to make atmospheric measurements [11]. In order for atmospheric parameters to be retrieved from the data from these lidar instruments (which measure only attenuated backscatter), many assumptions must be made. Klett and Fernald proposed lidar data inversions requiring assumptions of boundary extinction values, or an altitude invariant extinction to backscatter ratio [12, 13].

By observing the spectral properties of lidar returns in addition to the attenuated atmospheric backscatter, various atmospheric properties can be retrieved such as wind-speed, and extinction and backscatter coefficients, without the assumptions required for the Klett and Fernald retrievals [14, 15, 16, 11]. When atmospheric scatterers are in motion relative to a lidar instrument, the resulting scattered light experiences a Doppler shift in frequency associated with the component of that motion which is parallel to the path of the lidar transmitter beam. This technique can be used to monitor wind speed and direction (through judicious scanning of the lidar instrument), and is useful for studying the transport of aerosols through the atmosphere, and cloud formation.

High Spectral Resolution Lidar

High spectral resolution lidars (HSRLs) use a narrow-band optical filter to separate light that has been scattered by atmospheric aerosols from light that has been scattered by atmospheric molecules [14, 15, 16, 11]. This is possible because the light that has been scattered by molecules differs spectrally from that which has been scattered by aerosols. Due to the thermal motion of the air molecules, light that has

been scattered by those molecules experiences a doppler shift in frequency. When this occurs on a scale encompassing many scattering events, the net result is a broadening of the spectrum of the incident light. Due to their greater mass, and therefore slower thermal motion, atmospheric aerosols do not impart a significant Doppler broadening of the spectrum of incident light. The spectra of the aerosol and molecule scattered light can therefore be partially separated using a narrow band optical filter. The separated molecular and aerosol lidar return signals can be used in conjunction with a molecular scattering model to compute the aerosol extinction and backscatter coefficients. These coefficients are widely used, though difficult to measure, aerosol optical properties. Unlike simple backscatter lidar instruments, HSRL instruments are capable of providing atmospheric parameters such as extinction and backscatter without the assumptions required for the Klett and Fernald inversions of constant lidar ratio, etc.

Previous HSRL instruments have utilized either flat-plate interferometers, or gas absorption cells to separate the aerosol and molecular return signals [15, 16, 14, 17, 18]. The gas absorption cells typically are used to attenuate the central aerosol peak to nearly zero, while passing the wings of the Doppler broadened molecular signal. This effect is depicted in figure 3. However, there are drawbacks to each of these techniques. Barium gas filters have been used in several previous HSRL designs [11, 19]. The gas must be heated precisely to effectively filter the lidar return signal, and the Barium absorption feature which is commonly used, 553.7 nm, is not a convenient laser wavelength. Previous HSRL instruments utilizing Barium gas filters have used dye lasers locked to the Barium absorption line as transmitters. Iodine absorption filters can be operated at lower temperatures, and have a suitable absorption feature at the popular frequency-doubled Nd:YAG wavelength of 532 nm [11]. This makes iodine absorption cells a popular choice for separating molecular and aerosol returns

in HSRL instruments. The key disadvantage of using gas absorption cells in HSRL instruments is that they severely limit the possible wavelengths at which the HSRL can operate. One way to circumvent this problem is to use an interferometer as the filter in the HSRL. In the past, flat-plate Fabry-Perot interferometers have been used for this purpose [15]. They are theoretically portable to any wavelength. However, flat-plate interferometers must be very precisely aligned to work properly, which presents a serious challenge when working with multi-mode light from a telescope in a potentially mobile lidar instrument. Additionally, flat-plate interferometers must be very large to accommodate the multi-mode, wide angle light from a telescope in a lidar instrument. Due to its geometry, the confocal Fabry-Perot interferometer (CFP) is much less sensitive to small changes in alignment than flat-plate interferometers, and also accepts a wider cone of incident light, making it better suited for use in lidar instruments than a flat-plate interferometer [20, 21, 22, 23]. It can also be much smaller than a flat-plate interferometer when used with multi-mode incident light. Like a flat-plate interferometer, a CFP is theoretically portable to any desired wavelength. The work described in this dissertation was funded partly in an effort to develop a new satellite-ready HSRL instrument. Gas absorption cells are not well suited to space flight since any sort of leak or precipitate or vapor formation would render the cells useless, and their temperature must be carefully regulated. Flat plate interferometers are not practical for any sort of mobile application since they must be impractically large to meet the optical requirements for use in a lidar instrument, and are very sensitive to small alignment errors and vibrations. The CFP is ideal for use in a potential space-based instrument because it lacks the problems associated with gas cells, and is much smaller and less sensitive to alignment and vibration than a flat-plate interferometer.

An HSRL instrument has been designed and constructed at Montana State

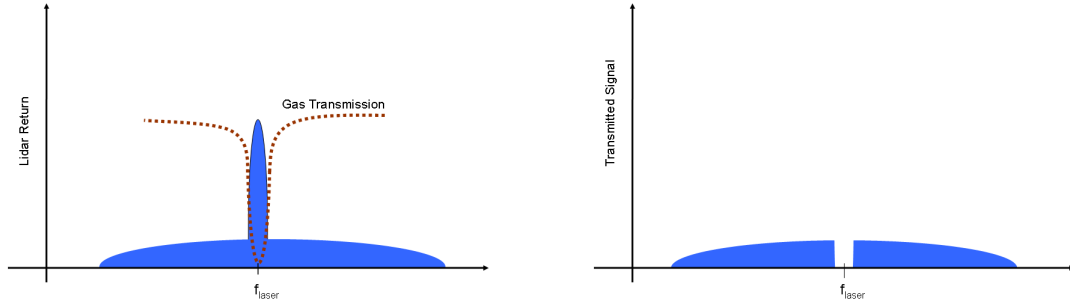


Figure 3: A gas absorption feature (Iodine is frequently used in HSRL instruments) overlays a plot of the spectral profile of a lidar return on the left. The central aerosol peak is blocked by the gas, leaving the molecular ”wings” seen in the right-hand plot.

University which utilizes a CFP to separate lidar returns from atmospheric aerosols and molecules. This type of filter was chosen due its previously described ability to accept wide-angle, multi-mode incident light. The filter was designed and fabricated to have optimal optical properties for use in an HSRL instrument. An analog frequency locking circuit was constructed to control the spacing of the CFP mirrors to ensure that the CFP maintains resonance at the laser-transmitter frequency. The CFP therefore passes the aerosol return signal, while rejecting the Doppler broadened molecular signal. The CFP is frequency-locked to the 1064 nm cw seed laser, and is simultaneously resonant at the first harmonic 532 nm wavelength. The CFP filter as used in the HSRL described in this dissertation represents a step forward in lidar technology in that it is a robust interferometer that is portable to any desired wavelength (the CFP could be frequency locked to any laser-transmitter wavelength).

The purpose of the HSRL instrument presented in this dissertation is to observe the optical properties of aerosols present in the atmosphere, which are important factors in the planetary radiation budget. The novel use of the CFP as a narrow-

band filter in the instrument allows for the construction of HSRL instruments utilizing arbitrary laser-wavelengths. This CFP is more robust than previously used flat-plate interferometers, allowing for construction of a potentially field-deployable HSRL. The CFP is portable to arbitrary wavelengths, unlike previously used molecular absorption filters, allowing for development of future multi-wavelength instruments [24]. This dissertation contains a description of the lidar instrument, a theoretical discussion of aerosol property retrievals, atmospheric data collected using the instrument, and an error analysis discussion. Much of this work is also presented in a manuscript which has been accepted by the Journal of Applied Optics [25].

HSRL INSTRUMENT

HSRL Instrument Layout

The HSRL instrument described in this paper is similar to the basic lidar instrument described by figure 2 in the introduction, with additional complexity added due to the need to separate aerosol and molecular lidar returns. A flow-diagram describing the operation of the instrument is shown in figure 4. A 1064 nm seed laser (1) supplies light to seed the Nd:YAG pulsed laser (2) and to frequency lock the CFP (7). To accomplish this frequency locking, some of the light from the seed laser (1) is picked off via an inline fiber splitter, frequency modulated (5), and is then incident on the CFP (7). The 1064 nm output of of the CFP (7) is monitored by a NIR detector (8), the output of which is used by the locking servo (9) to control the length of the CFP (7). While the CFP is frequency-locked to the seed laser, the output of the seeded, pulsed Nd:YAG laser (2) is incident on a frequency doubler (3). The resulting 532 nm light is sent to the atmosphere (4) where it is scattered by air molecules and aerosols. Some of the that scattered light is collected by a telescope (6), and is then incident on the CFP (7). The reflected and transmitted optical signals from the CFP are turned into electrical signals by visible detectors (8) which are then digitized and recorded by a computer (10).

A schematic depicting the HSRL instrument including the CFP is shown in fig. 5. The laser transmitter used in the HSRL is a Continuum Surelite series injection seeded Nd:YAG laser. 90% of the light from a 1064 nm seed laser is used to injection seed the pulsed laser amplifier, while 10% of the seed laser light is picked off via an inline fiber splitter and used to frequency lock the CFP to the seed laser wavelength. The CFP is locked to the seed laser using a frequency modulation technique. The

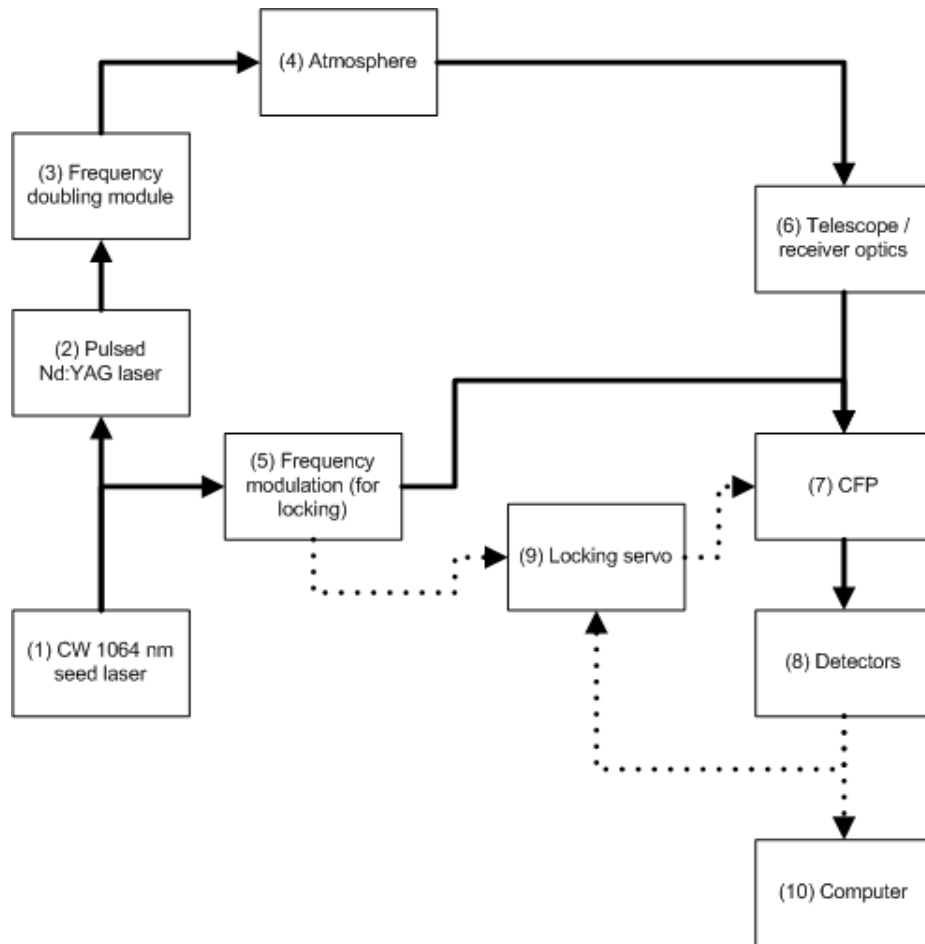


Figure 4: A flow diagram detailing the operation of the HSRL instrument.

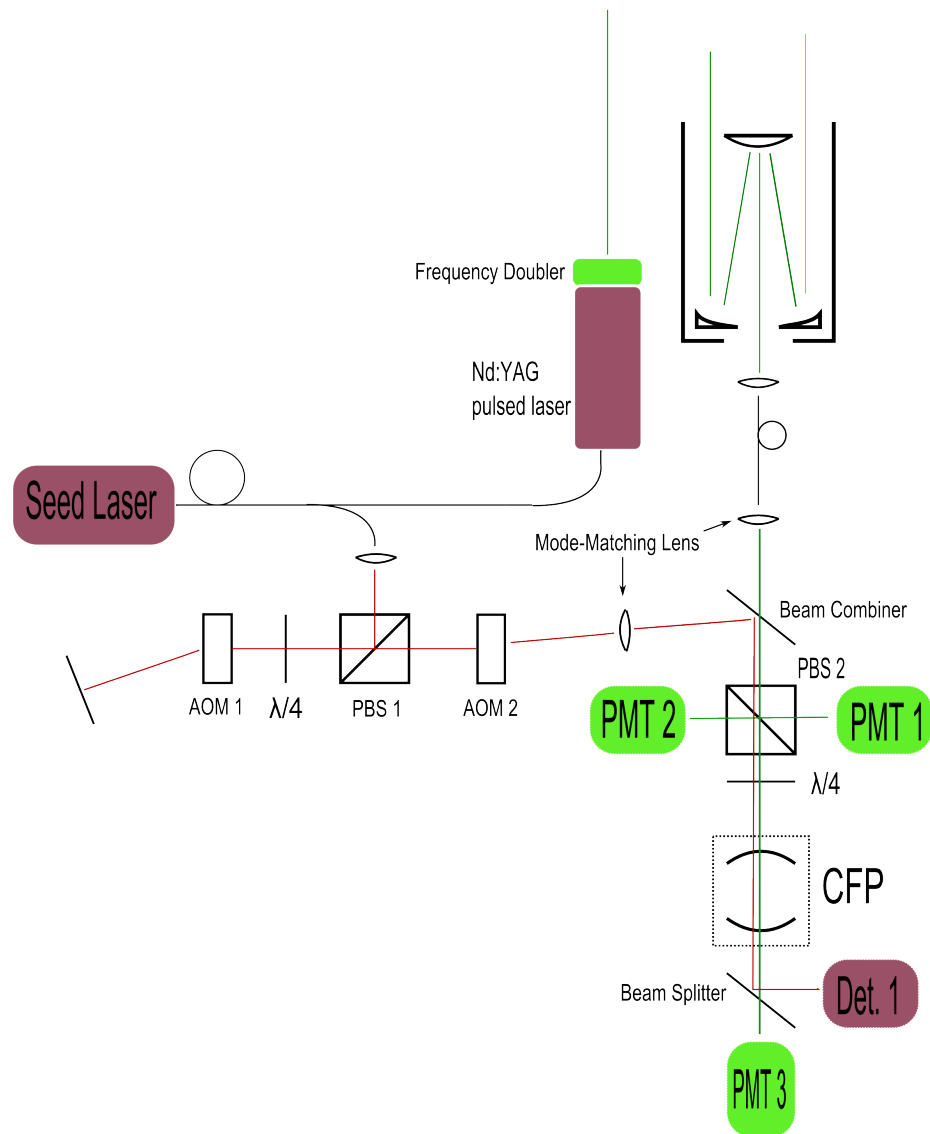


Figure 5: A schematic of the HSRL instrument.

Table 1: Transmitter and Receiver Parameters.

Parameter	Value
Seed Laser Power	44 mW
1064 nm Pulse Energy	360 mJ
532 nm Pulse Energy	160 mJ
Pulse Duration	7.5 ns
Pulse Repetition Rate	10 Hz
Laser Divergence	0.60 mRad
Receiver Field of View	1.24 mRad
Telescope Diameter	30.5 cm
CFP Mirror Spacing	1 cm
Receiver Fiber Diameter	200 μ m

1064 nm light from the seed laser that has been separated for locking is collimated and directed via a polarizing beam splitter (PBS 1) through an acousto-optic modulator (AOM 1) in a double-pass configuration. To accomplish this, the first-order diffracted output of AOM 1 is reflected back through the AOM, where it is refracted again such that the first order output overlaps the original incident beam. AOM 1 modulates the frequency of the incident light sinusoidally as controlled by an external electrical signal generator. The double-pass configuration allows for a larger frequency modulation amplitude than could be achieved with a single pass, while minimizing beam steering effects. A frequency offset is also produced by this process. After passing through PBS 1, the 1064 nm light is next incident on AOM 2, which removes the frequency offset introduced by AOM 1. The first order diffracted output of AOM 2 is incident on a mode-matching lens, and is then combined with 532 nm science channel light from a fiber by the beam combiner, and is then incident on the CFP. The portion of the modulated 1064 nm seed laser light that is transmitted by the CFP is directed by a dichroic beam splitter to a silicon photo detector (Det. 1) which converts the light to an electrical signal. This electrical signal is used to frequency-lock the CFP to the 1064 nm seed laser as will be discussed later in this chapter.

The injection seeded Nd:YAG laser outputs approximately 360 mJ of 1064 nm light with a pulse duration of 6 ns and a repetition rate of 10 Hz. This light is incident on a second-harmonic generator which outputs 160 mJ of 532 nm light, which is directed into the atmosphere. The linewidth of the second harmonic 532 nm light is less than 150 MHz. Backscattered, attenuated light from the atmosphere is collected by a 12 inch Schmidt-Cassegrain telescope, then launched into a 200 μ m, 0.22 NA optical fiber which delivers the light to the receiver optics assembly. 532 nm light from this fiber is incident on a lens which is used to mode-match the light to the CFP. The light is then combined with the 1064 nm locking light from the seed laser, and is then incident on polarizing beam splitter PBS 2. Approximately half of the randomly polarized 532 nm light is directed by PBS 2 to photomultiplier tube PMT 1, which records the total signal before the CFP. The remainder of the light is incident on the CFP. The transmitted 532 nm light is incident on PMT 3, which converts the transmitted light to an electrical signal. This transmitted signal represents light that has been scattered by atmospheric aerosols, which has experienced negligible Doppler broadening. Light that is rejected by the CFP is directed by PBS 2 to PMT 2, which converts the reflected light to an electrical signal. This reflected light represents Doppler-broadened light that has been scattered by atmospheric molecules. A 3 nm wide narrow-band filter is located at the input of all three PMTs, which reduces the amount of background light incident on the detectors. A summary of the HSRL parameters is given in table 1.

Confocal Fabry-Perot Interferometer

The CFP acts as a filter that separates the molecular lidar returns from the aerosol returns. The ability of the interferometer to effectively separate these returns is

dependent on its spectral response, which is in turn dependent on physical properties of the interferometer such as mirror reflectivity and spacing. Like any other Fabry-Perot interferometer, the CFP has a high transmission when a resonance condition inside the cavity is achieved, resulting in a standing wave between the cavity mirrors. Such a condition is achieved when an integer number of half-wavelengths of the incident light fit exactly between the mirrors, or

$$m\frac{\lambda}{2} = L, \quad (1)$$

where L is the cavity length, λ is the wavelength of the incident light, and m is an integer. A plot of theoretical interferometer transmission as a function of wavelength for a set mirror spacing is shown in fig. 6. The spacing between the transmission peaks, known as the free spectral range (FSR), is related to the mirror spacing, while the finesse, which refers to the relative width of the peaks compared to the free spectral range, is related to mirror reflectance. The relation

$$FSR = \frac{c}{2L}, \quad (2)$$

is valid for a single spatial mode incident light source that is mode-matched to the cavity, where c is the speed of light [26]. The finesse is dependent on the mirror reflectance:

$$F = \frac{\pi\sqrt{R}}{1-R}, \quad (3)$$

where R is mirror reflectance [26]. Fabry-Perot interferometers in the confocal configuration can be resonant for multimode light sources, which makes them highly applicable to use in lidar instruments due to the multi-spatial-mode nature of scattered light returning from the atmosphere. In the case of multi-mode resonance, the even and odd spatial modes add constructively into two distinct groups, which

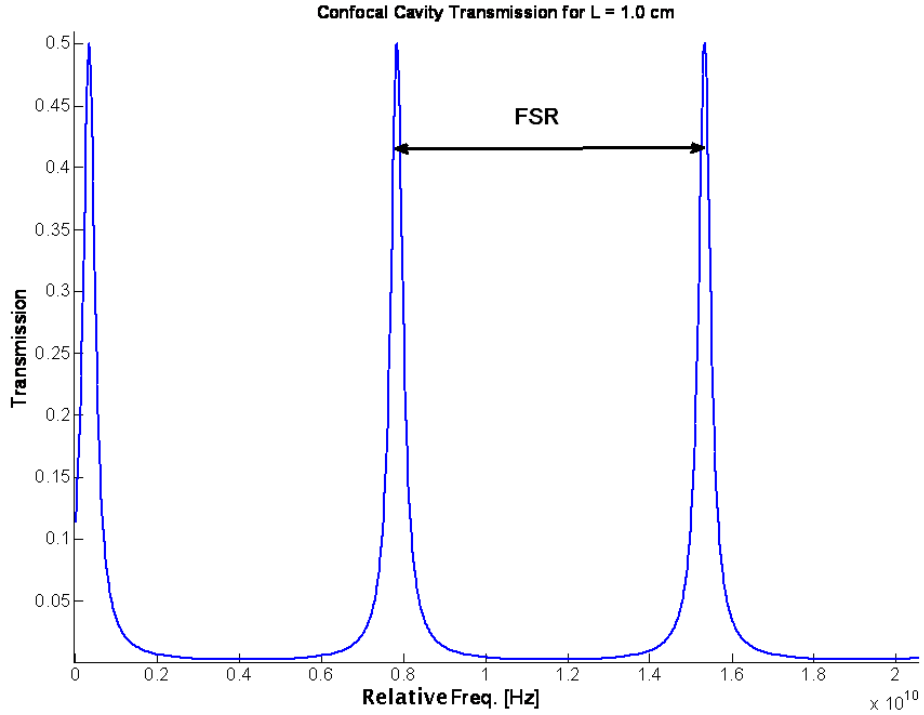


Figure 6: A plot of CFP transmission vs incident light frequency for a cavity length of 1 cm.

have half the spacing of a single resonant mode, and thus half the FSR [20]:

$$FSR_{CFP,multi-mode} = \frac{c}{4L}. \quad (4)$$

These multi-mode cavity resonance modes, which have half the FSR associated with the resonance modes for a single-mode incident light source, also have only half the amplitude, resulting in a theoretical maximum CFP transmission of 50% for multimode incident light.

The CFP used in the HSRL is frequency locked to the seed laser wavelength, making it resonant (thus having high transmission) at the center wavelength of light that has been back-scattered by atmospheric aerosols. Transmission is much lower for the Doppler-broadened light that has been scattered by atmospheric molecules. This

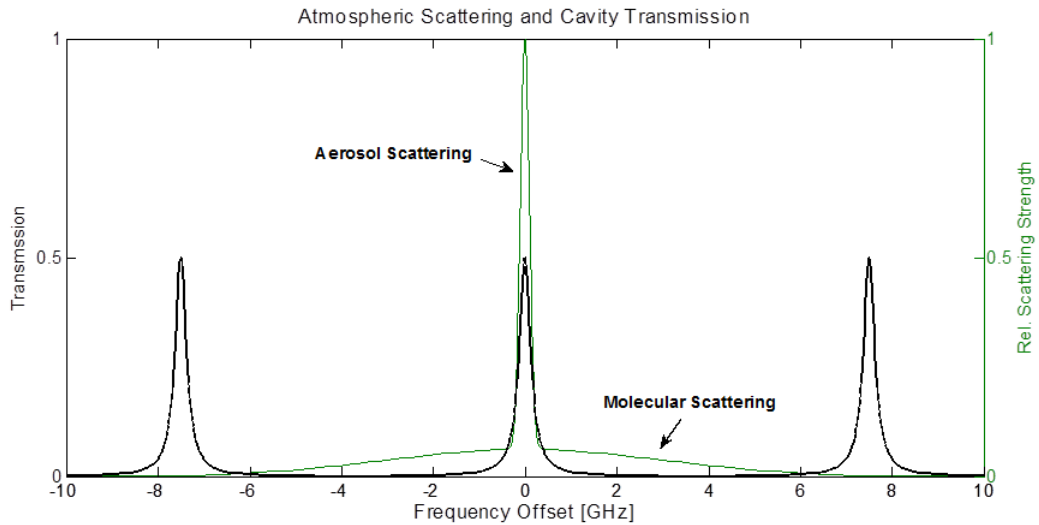


Figure 7: A plot of CFP transmission compared to the spectral distribution of light backscattered by the atmosphere. The CFP transmitted most of the central aerosol peak, while reflected most of the molecular ”‘wings.’”

effect is depicted in figure 7, and will be discussed further in the next section. This difference between CFP transmission of aerosol scattered light and CFP transmission of molecule-scattered light allows the molecular and aerosol components of each lidar return to be calculated based on the detected light transmitted and reflected by the CFP.

CFP Design

The mirrors used in the CFP interferometer in the optical receiver of the HSRL shown in figure 5 have a radius of curvature of 1 cm yielding a $FSR_{mm} = 7.5$ GHz. The mirrors are constructed of fused silica, and have a dielectric coating (applied by Rocky Mountain Instrument Company) to ensure proper reflectivity at 532 and 1064 nm. The mirror reflectance at the 532 nm (1064 nm) wavelength is $R = 94\%$ (99%) resulting in a finesse of 50.7 (312). Dividing the free spectral range $F=c/2Rc = 15$ GHz

by the finesse at the 532 nm second harmonic wavelength of 50.7 yields a bandpass for the CFP of 300 MHz, which is twice the laser linewidth at the second harmonic wavelength for the laser transmitter. A theoretical plot of the CFP interferometer transmission as a function of relative frequency is shown as the solid black line in figure 7, where a mirror absorption of $A = 0$ was assumed. A plot of the total scattered signal as a function of relative frequency is shown as the green line in figure 7 where contributions to the scattered signal from the spectrally narrow Mie scattered light and the Doppler broadened Rayleigh scattered light can be seen. The effect of different mirror reflectivities on normalized CFP transmission can be seen in figure 8. The reflectivity of 94 % was chosen because it results in a pass-band wide enough to pass most of the light from the laser-transmitter, while rejecting most of the Doppler broadened, molecularly scattered wings. The FSRmm of the CFP interferometer is large enough that the transmission of the Doppler broadened molecule-scattered light by adjacent transmission peaks of the CFP interferometer are minimal. The 1 cm mirror spacing between the CFP mirrors is just small enough to avoid such overlap, while also allowing the CFP to be physically large enough to effectively accept the large-angle multimode light collected by the telescope in the HSRL instrument.

A schematic of the CFP designed to house the mirrors described above is shown in figure 9. The right hand mirror is held in an aluminum flange. An insulating flange made from delrin abuts the aluminum flange and provides a seat for the 2.54 cm diameter piezoelectric transducer (PZT) tube used to scan the CFP for cavity characterization and used along with the locking servo to lock the CFP to the HSRL laser transmitter as discussed in the next section. The left hand side of the PZT tube is seated in a second insulating flange that abuts a second aluminum flange. This tube assembly is held together with three $\frac{1}{4}$ – 20 bolts placed 120° apart. O-rings placed between the $\frac{1}{4}$ – 20 nut and right hand aluminum flange allow the cavity to scan freely

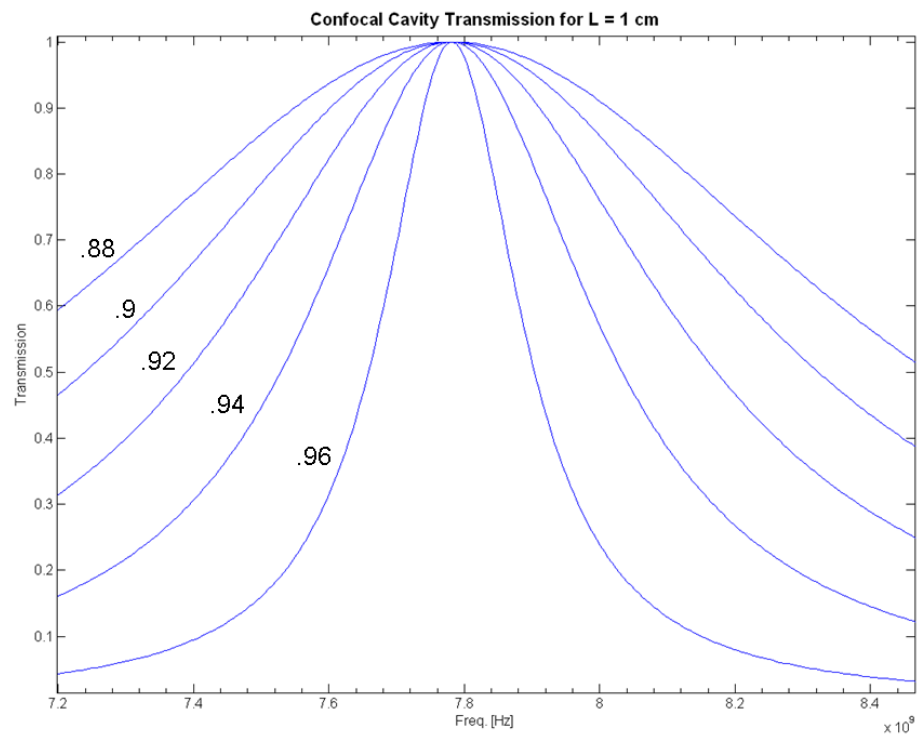


Figure 8: Normalized theoretical CFP transmission for mirror reflectivities .88 - .96.

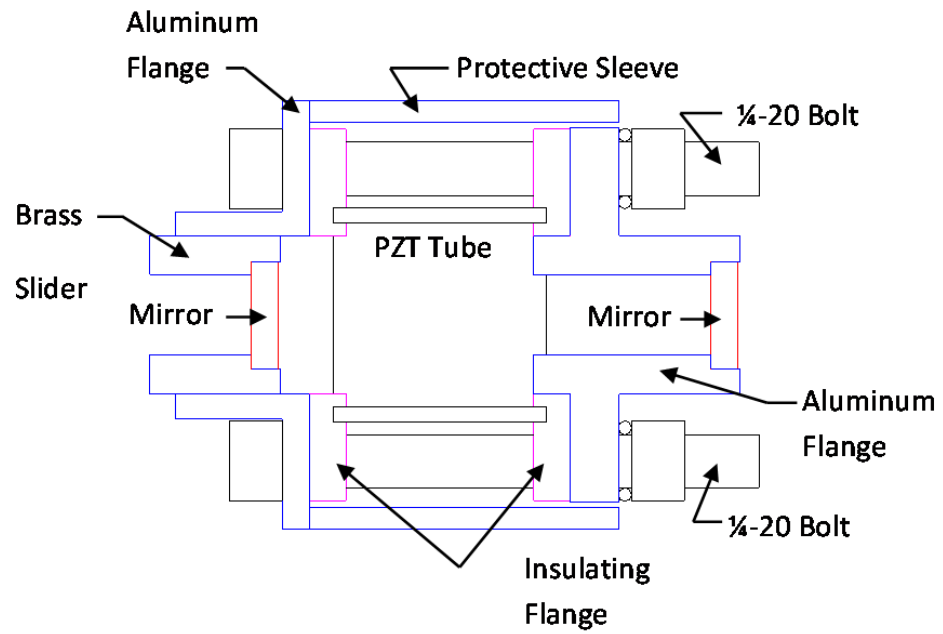


Figure 9: The mechanical layout of the CFP used in the HSRL instrument.

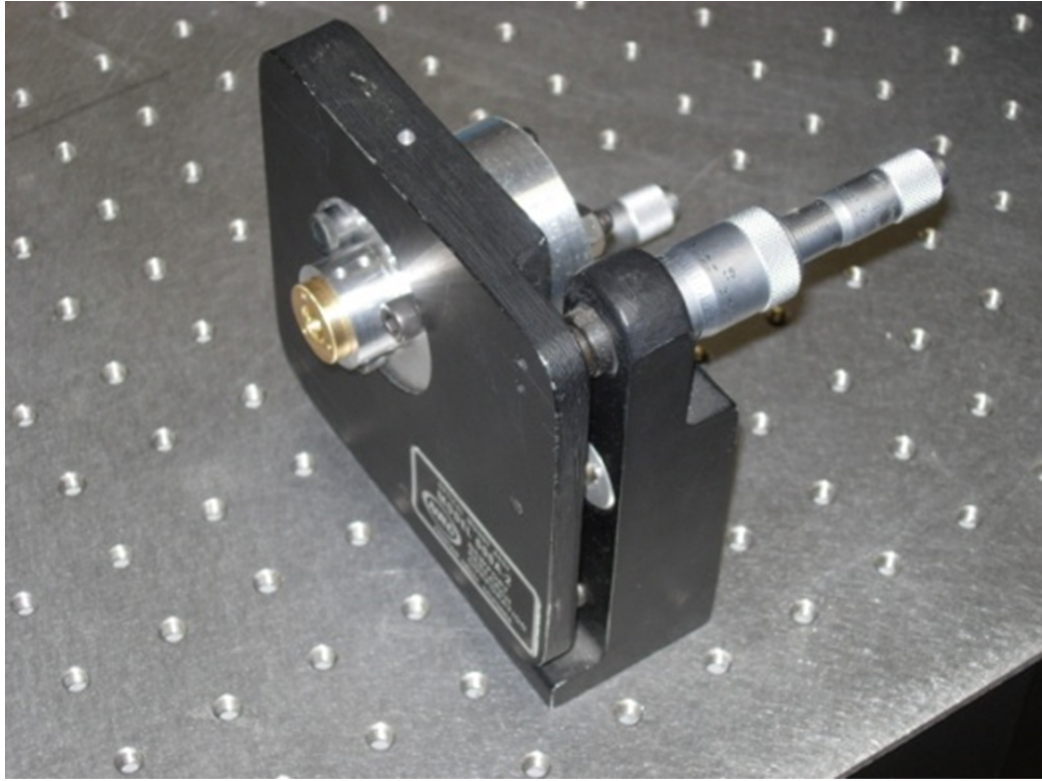


Figure 10: A photo of the CFP used in the HSRL instrument.

via the PZT tube. A protective sleeve with a 5.08 cm outside diameter is attached to the left hand aluminum flange allowing the CFP to be mounted in commercial stages. The left hand mirror is mounted in a brass slider tube that fits within the left hand aluminum flange which allows adjustment of the CFP cavity length while the cavity is scanning so that the cavity mode structure can be monitored. This allows adjustment of the cavity spacing to achieve the confocal cavity condition. Once the confocal cavity condition is met, the brass slide is locked down with three set screws. A photograph of the confocal cavity is shown in figure 10.

An experiment was conducted to determine an acceptable layout of the CFP in relation to the incident light from the telescope in the HSRL, with the physical layout used for this experiment shown in figure 11. 532 nm light from a frequency-doubled

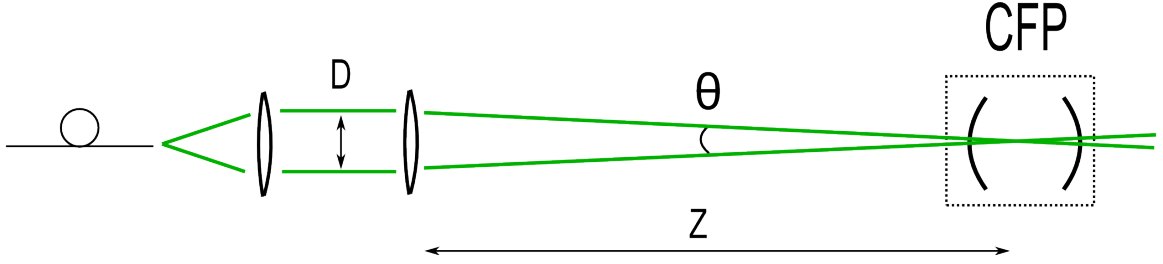


Figure 11: The configuration used to test the optimal positioning of the cavity to filter multimode light from a $200\ \mu\text{m}$ fiber.

Nd:YAG laser was launched into a $200\mu\text{m}$ multi-spatial-mode fiber. The light exiting this fiber was incident on two lenses which focused the light at the center of the CFP, with a beam diameter, 'D,' of 2.6 cm being maintained at the second lens. The distance, 'Z,' between the second lens and the CFP was varied, thus also varying the angular content of the light incident on the CFP, and the resulting cavity finesse was calculated based on the shape of the cavity transmission signal while the cavity length was mechanically scanned. Finesse can be represented by

$$F = \frac{BW}{FSR}, \quad (5)$$

where BW is the width of a transmission peak at half its maximum value, and FSR is the free spectral range, or spacing between the transmission peaks. Figure 12 shows these finesse results with their corresponding 'Z' distances. Cavity finesse is seen to increase with distance (decrease with angle) until a plateau is reached at 30 cm. A slightly lower plateau appears starting around 48 cm, and the finesse drops off around 70 cm. Beyond $Z = 70$ cm, the cavity throughput dropped off enough that finesse was difficult to reliably measure. At small 'Z' distances, the beam spot size is small, and finesse is dependent on the incidence angle of the incident light. As the angle becomes smaller, the finesse grows until the mode-matched condition is approached [27]. This occurs when the curvature of the incident beam matches that of the mirrors in the CFP at the point where the beam meets the mirror's surface. At this point, the finesse

stops increasing with increasing distance (and decreasing angle) because the spot size of light has become large enough that spherical aberrations due to the spherical cavity mirrors start to offset the effects of decreasing the angle. As the distance 'Z' continues to increase, the spherical aberrations continue grow and eventually cause the finesse to decrease [28]. Based on this experiment, an acceptable range of distances between the focusing lens and the CFP (assuming a 2.6 cm beam diameter at the focusing lens) was decided to be between 30 and 45 cm. Based on physical constraints such as the desired size of the HSRL instrument, as well as available lens focal lengths, a distance of 38 cm was chosen for the completed instrument. A 2.6 cm beam diameter at the focusing lens was maintained to ensure the angular content of the light incident on the CFP was consistent with that found in the experimental setup.

Locking

A frequency locking servo has been developed to control the length of the CFP based on the 1064 nm seed laser such that it is resonant at the desired second and third harmonic wavelengths of 532 and 355 nm. Because 532 nm and 355 nm light have double and triple the frequency of 1064 nm light respectively, if the cavity is resonant at 1064 nm, it will also be resonant at 532 and 355 nm, as shown in figure 13, assuming the use of ideal mirrors. However, the highly efficient dielectric coatings used in the CFP cause the harmonic frequencies to experience a slightly different mirror spacing than that experienced by the 1064 nm light. The transmission peaks at the different wavelengths therefore do not line up exactly. Dispersion due to the non-vacuum conditions between the cavity mirrors also contributes slightly to this effect. The frequency modulation stage of the cavity-locking optical train is used to correct this offset by adjusting the frequency of the 1064 nm light so that it is

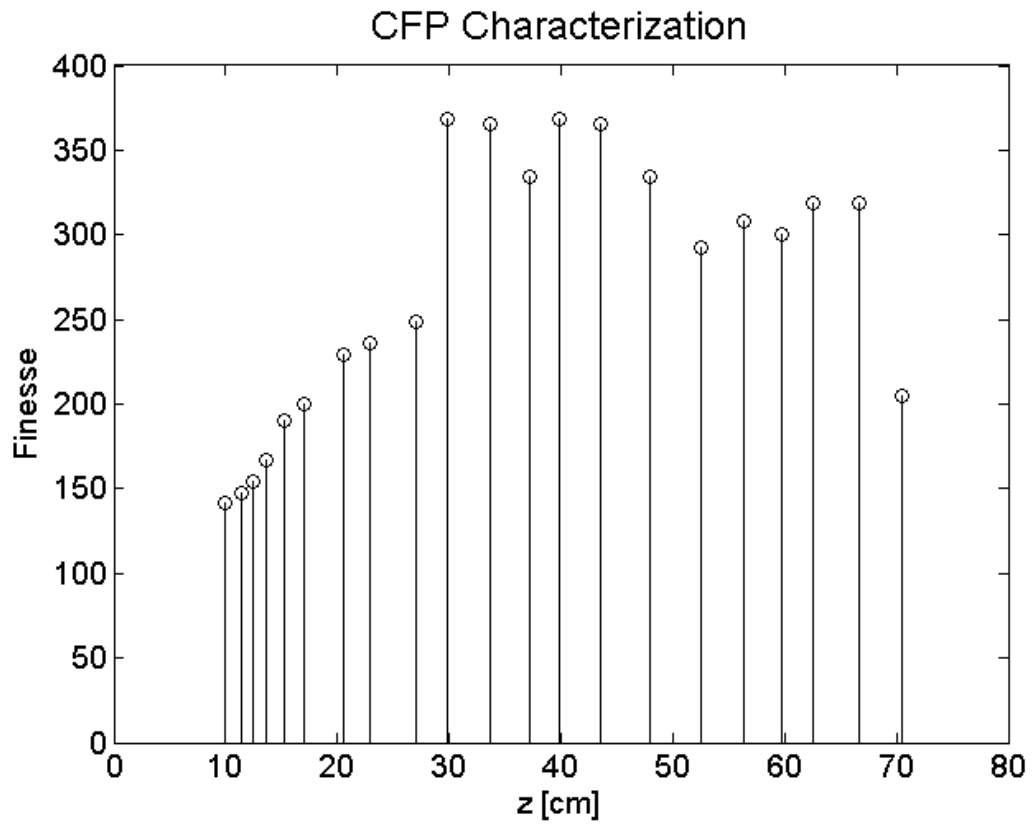


Figure 12: A plot of CFP finesse vs distance Z between lens 2 (see figure 11) and the CFP. The angular content of the incident light is a function of distance Z , and beam diameter at lens 2 D.

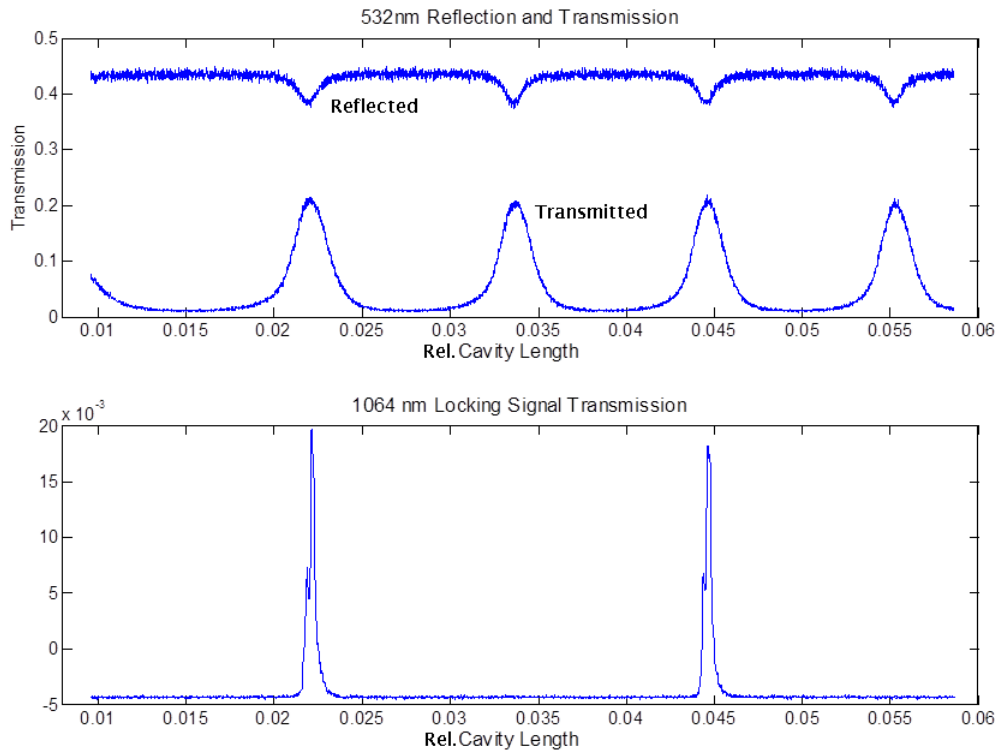


Figure 13: A plot of CFP transmission and reflectivity while the cavity length is scanned via piezo-electric transducer. The top plot is CFP reflectivity and transmission at 532 nm, and the bottom plot is 1064 nm transmission. The small side-lobe in the 1064 nm signal is present because the 1064 nm beam has been aligned for perfect resonance overlap with the 532 nm signal, rather than high finesse.

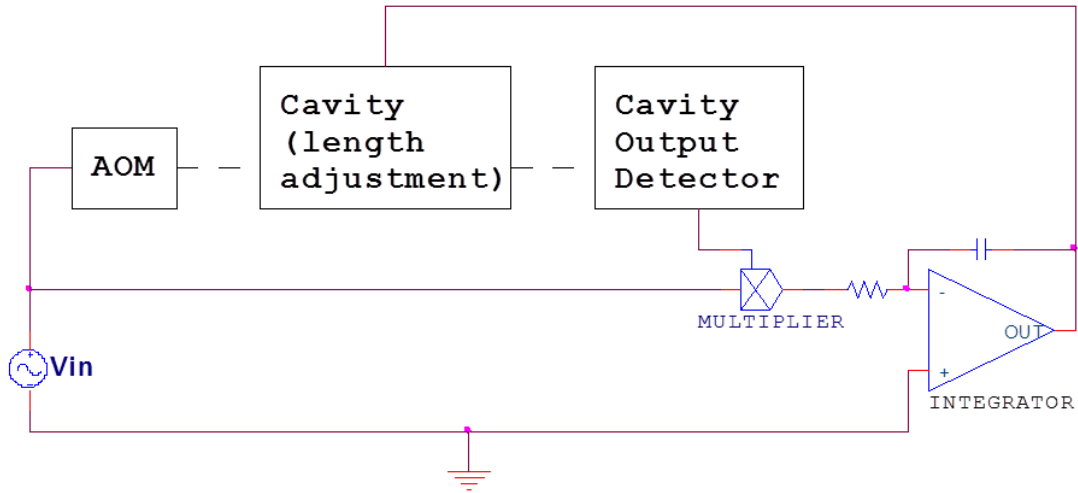


Figure 14: A flow diagram depicting the locking of the CFP to the 1064 nm seed laser. The dashed lines represent an optical signal traveling from the AOM through the CFP to the 1064 nm detector, while the solid lines represent electrical signals.

co-resonant with the 532 nm science channel light. Figure 5 shows how the confocal interferometer and locking system are incorporated into the HSRL.

The confocal cavity interferometer is locked to the seed laser via an active feedback analog control circuit (see figure 14). Reference 1064 nm light from the seed laser is incident on an acousto-optic modulator (AOM 1); the first order diffracted output is then retro-reflected back into AOM 1 producing a first-order diffracted output beam that is overlapped with the original input beam. Double passing AOM 1 in this manner imparts a frequency modulation, which is proportional to the sinusoidal analog voltage signal applied to AOM 1, on the 1064 nm locking light. The center-frequency of this modulation is approximately 80 MHz (40 MHz per pass), with an amplitude of approximately 10 MHz. Additionally, a small parasitic frequency offset is produced. The frequency modulated 1064 nm light is next incident on AOM 2, which corrects the frequency offset introduced by AOM 1 by inducing an approximately 80

MHz frequency shift opposite in magnitude to the original shift induced by AOM 1. A small part of the original offset is left in place to account for the previously discussed frequency offset between the 532 nm and 1064 nm CFP resonances. This offset allows the 532 nm science channel light and the 1064 nm locking light to be co-resonant despite phase shifts due to dielectric mirror coatings and dispersion due to the air in the cavity. The first order output of AOM 2 is a frequency-modulated 1064 nm beam centered on the original seed-laser frequency. This beam is introduced to the receiver-optics train, overlapped with the 532 nm science-beam, and is eventually incident on the CFP. The transmission of the reference light through the CFP is modulated due to the frequency dependence of the cavity transmission. An analog electronic circuit uses the AOM 1 analog voltage signal (proportional to the applied frequency modulation) and the resulting cavity transmission signal to modify the length of the cavity such that it is resonant at the mean frequency of the modulated optical reference (the 1064 nm seed laser frequency). The cavity output signal and the sinusoidal signal used to drive AOM 1 (which has a mean value of zero volts) are multiplied together; the result is integrated over many periods to produce an error signal that is used to adjust the length of the cavity. As seen in figure 15, if the cavity is too long, a positive error signal is produced which acts to shorten the cavity length. If the cavity is too short, a negative error signal is produced which acts to lengthen the cavity. If the cavity is the correct length, an error signal of zero volts is produced which does not affect the cavity length. This is possible because as the cavity becomes longer, the cavity transmission peak is pushed toward the positive part of the sinusoidal AOM control signal so that when the two signals are multiplied, the result has a positive mean value. As the cavity becomes shorter, the transmission peak is pushed toward the negative part of the AOM control signal so that when the two signals are multiplied, the result has a negative mean value. A photograph

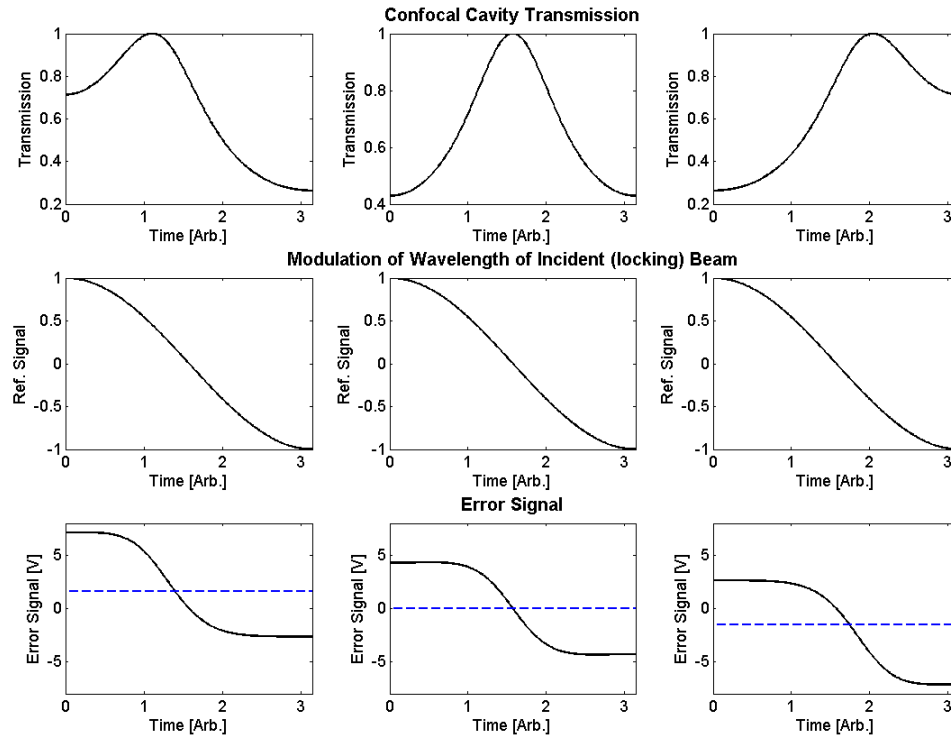


Figure 15: Cavity transmission, AOM drive signal (proportional to incident light wavelength shift) and resulting error signal for three different cavity lengths. The column on the left corresponds to an oversized cavity, the column on the right corresponds to an undersized cavity and the center column corresponds to the desired cavity length. Note that these signals are plotted over $\frac{1}{2}$ period of the reference sinusoid that drives the AOM. The other $\frac{1}{2}$ period is a reflection of these plots and has been omitted for simplicity.

showing the layout of the optical components used in the frequency locking process is shown in figure 16. The red line represents the 1064 nm optical path, while the green line represents the 532 nm optical path.

The frequency locking servo which controls the mirror spacing in the CFP to maintain resonance of the seed laser wavelength is diagrammed in figure 17. This circuit provides the functionality described in figure 14. The 1064 nm seed laser is frequency modulated, and is then incident on the CFP. The laser seed laser light which

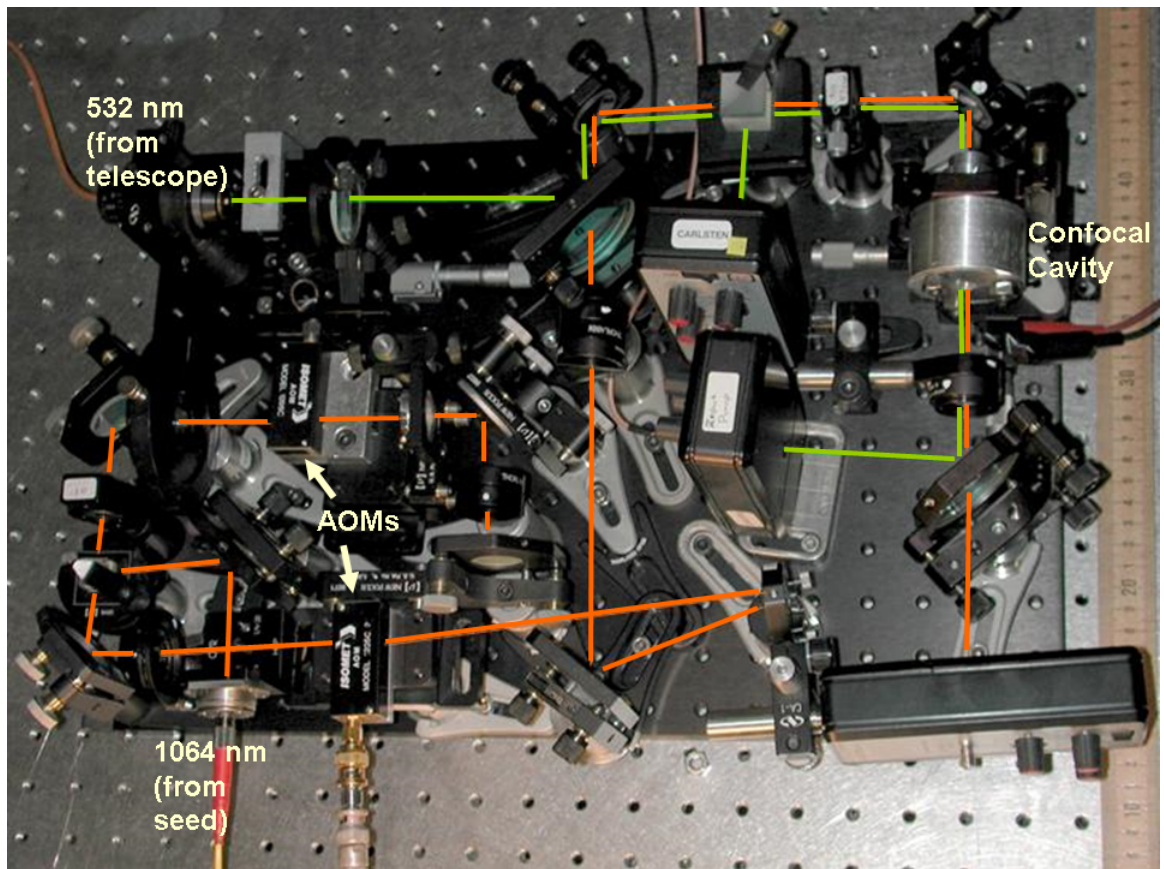


Figure 16: A photo of the locking optical train. The green lines represent the green science channel light, while the red lines represent the 1064 nm light from the seed laser used to lock the cavity. The green channel detectors have been replaced with PMTs for use in data collection.

is transmitted by the CFP is therefore amplitude-modulated due to the frequency dependence of the CFP transmission. This seed laser transmission signal is multiplied by a signal which is proportional to the original sinusoidal frequency modulation of the seed laser. The result of this multiplication is integrated over several periods, is then amplified to an appropriate level, and is added to a DC signal which controls the mirror spacing within the CFP. The frequency modulation reference signal and the cavity transmission signal enter the circuit at BNC inputs J1 and J2 respectively. The transmission signal is amplified by Op-Amp U6, and is then incident on the AD633 multiplier U1. The frequency modulation reference signal is attenuated via a trim-potentiometer and Op-Amp U2. Residual DC noise is removed by capacitor C3, after which an adjustable DC signal is added by Op-Amp U3. This DC signal allows the sinusoidal reference signal to be carefully centered around 0 volts, which is critical to the proper operation of the locking circuit. The reference signal is multiplied by the CFP output signal via the AD633 multiplier U1. This multiplied signal is next incident on the integrator circuit which utilizes Op-Amp U4. The output of the integrator is amplified by Op-Amp U5, and is then added to an adjustable DC offset signal and further amplified by high-voltage Op-Amp U7. The offset signal introduced here allows the CFP mirror spacing to be manually scanned in order to find an appropriate resonance feature for frequency locking. The output of Op-Amp U7 is used to drive the piezo-electric tubes which mechanically control the mirror spacing within the CFP. Not shown in the diagram is a momentary switch which allows the integrator to be shorted while the cavity length is scanned via potentiometer R22.

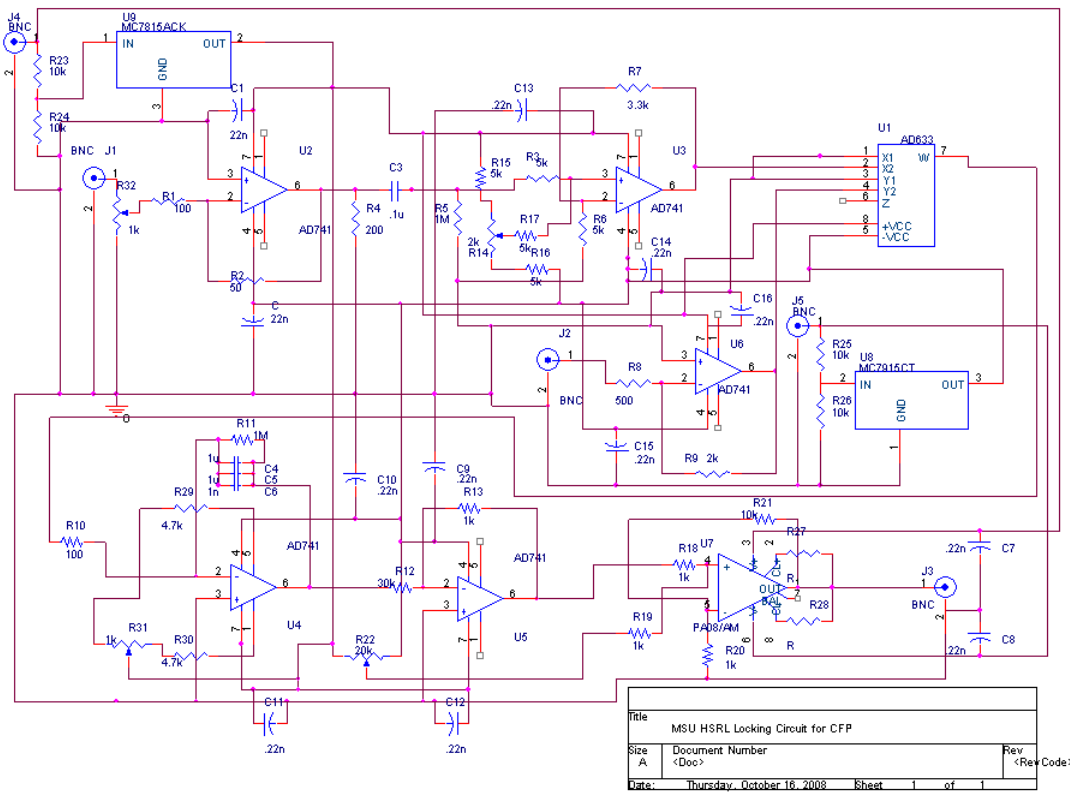


Figure 17: A circuit which actively maintains the mirror spacing within the CFP such that the CFP remains resonant at the 1064 nm seed laser wavelength.

Data Acquisition

The HSRL is operated through an opening in the roof of the laboratory allowing access to the atmosphere. Transmitted and reflected lidar returns -representing light that has been transmitted through the cavity, and light that has been reflected by it respectively -are recorded via a 14-bit, 200 MHz digitizer at a pulse repetition rate of 10 Hz. The digitizer has a 50 ohm input impedance to convert the current output from the PMTs in the HSRL instrument into a voltage signal prior to digitization. This is the desired impedance specified for the PMTs used to maintain an appropriate bandwidth while maximizing the resulting voltage signal. A 100 MHz low-pass filter is applied to the signal before digitization to prevent aliasing. Throughout data collection, the CFP is actively frequency locked to the seed laser, providing the stable narrow band filter required for the successful HSRL operation. A ten-return hardware averager is applied before the data are saved on a hard-drive. Data are typically collected for 1-2 hours at a time with short sections of data collected on either end with the telescope blocked for the purpose of background electronic noise estimation. A flow diagram of the data acquisition process is shown in figure 18.

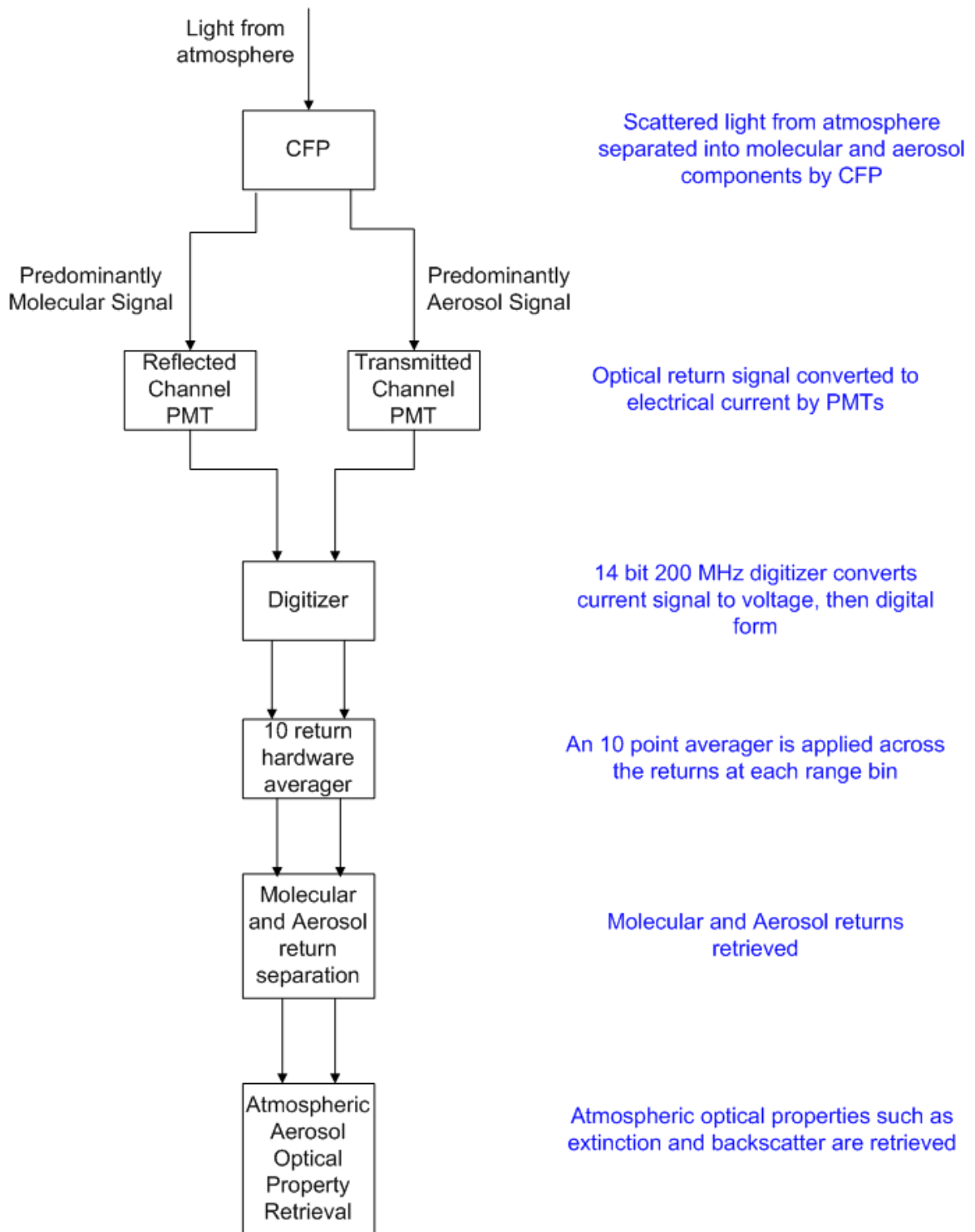


Figure 18: A flow diagram of the data acquisition process.

THEORY AND DATA ANALYSIS

The backscattered light received by a lidar instrument at any given time can be represented as a function of the light transmitted by the lidar attenuated by various factors and delayed by the round-trip travel time of that light. The basic lidar equation describes the optical power received by the lidar instrument, $P_\lambda(r)$, from a range of r , as [10]

$$P(r) = P_t \frac{A}{r^2} \frac{c\tau}{2} \beta(r) e^{-2 \int_0^r \sigma(r') dr'} \epsilon(\lambda) \epsilon(r), \quad (6)$$

where P_t is the laser transmitter pulse power, A is the area of the lidar receiver's light collection optics, c is the speed of light, τ is the laser pulse duration, $\beta(r)$ is the backscatter coefficient, $\sigma(r)$ is the extinction coefficient, $\epsilon(\lambda)$ is the spectral transmission of the receiver optics at wavelength λ and $\epsilon(r)$ is the overlap function. The overlap function, $\epsilon(r)$, refers to the overlap between the field of view of the telescope and the intensity profile of the laser as a function of range. The extinction coefficient, $\sigma(r)$, represents the amount of light emitted by the lidar instrument that experiences scattering, absorption, or other phenomena at range r that prevents it from propagating to further ranges. The integration of the extinction coefficient from range 0 to range r multiplied by 2 represents the total amount of light absorbed, scattered, or otherwise impeded while traveling from the lidar instrument to range r and back again. Taking this factor into account allows for meaningful study of a particular range, while eliminating as much as possible the influences of conditions between the lidar instrument and that specific range. The backscatter term, $\beta(r)$, represents the light scattered at range r in a backward direction such that the light is sent back toward the lidar instrument.

The goal of the HSRL technique is to separate the lidar return signal into two components; one that is due to aerosol scattering and one that is due to molecular scattering. Ideally, the narrow-band aerosol returns would pass through the cavity, while the Doppler-broadened molecular returns would be reflected. However, in reality, the light that passes through the cavity is a linear combination of aerosol and molecular returns, as is the light that is reflected [16]. This effect can be overcome by characterizing, for both light scattered by molecules and light scattered by aerosols, the amount of incident light that is reflected and the amount that is transmitted by the cavity. The amounts of incident molecule-scattered light and aerosol-scattered light can be calculated from measurements of the light that is transmitted and reflected by the cavity as follows,

$$P_{0,M}(r) = \frac{\frac{D_M(r)}{\gamma_M} - \frac{K_{A,M}D_A(r)}{\gamma_A(r)K_{A,A}}}{K_{M,M} - \frac{K_{M,A}K_{A,A}}{K_{A,A}}}, \quad (7)$$

$$P_{0,A}(r) = \frac{\left(\frac{D_A(r)}{\gamma_A} - \frac{K_{M,A}D_M(r)}{\gamma_M K_{M,M}}\right)}{\left(K_{A,A} - \frac{K_{A,M}K_{M,A}}{K_{M,M}}\right)} \quad (8)$$

where $P_{0,M}$ is the incident molecular-light, $P_{0,A}$ is the incident aerosol-light, D_A is the detected light in the aerosol (transmitted) channel, D_M is the detected light in the molecular (reflected) channel, γ_M is the efficiency of the molecular channel detector, γ_A is the efficiency of the aerosol channel detector, $K_{A,M}$ is the proportion of aerosol light detected in the molecular channel, $K_{A,A}$ is the proportion of aerosol light detected in the aerosol channel, $K_{M,A}$ is the proportion of molecular light detected in the aerosol channel, and $K_{M,M}$ is the proportion of molecular light detected in the molecular channel [16]. The K and γ values for the HSRL system are determined by making two measurements of the cavity. First, an attenuated pulse of 532 nm light from the HSRL laser source is launched into the cavity, and measurements of reflected and transmitted light are made to calculate $K_{A,A}$ and $K_{A,M}$. The calculation is

performed in this manner because the spectrum of the laser is not significantly altered by its transit through the atmosphere nor its scattering by atmospheric aerosols. To calculate $K_{M,A}(r)$ and $K_{M,M}(r)$, a narrow-band, continuous wave laser source is launched into the cavity and the length of cavity is scanned while the reflected and transmitted optical signals are recorded. This provides a spectrally resolved plot of cavity transmission and reflection (see fig 13). This cavity frequency response is then multiplied by a range resolved, modeled, molecularly scattered optical signal (in the frequency domain), and the result integrated to produce the $K_{M,A}$ and $K_{M,M}$ values used in equation 8. The modeled molecular signal is the convolution of the outgoing laser spectrum and a frequency-spread function that implements the effects of Doppler broadening due to molecular scattering. As presented by Shipley et al., this Doppler broadening function is given by [16],

$$D(\sigma, T_k) = \sqrt{\frac{\bar{m}c^2}{8\pi\sigma_0^2 k T_k} e^{-\frac{\bar{m}c^2}{8\pi\sigma_0^2 k T_k} (\sigma - \sigma_0)^2}} \quad (9)$$

where σ is the wavenumber of the scattered light, σ_0 is the wavenumber of the incident light, T_k is atmospheric temperature (a function of altitude), c is the speed of light, and k is Boltzmann's constant [*5,*7]. Equation 9 describes Doppler broadening due to thermal motion of air molecules, which is a function of atmospheric temperature and therefore also a function of altitude. Simple atmospheric models can be used to provide range resolved temperature profiles for use in characterizing the confocal cavity interferometer. The temperature as a function of altitude h for 0 to 11 km (beneath the tropopause) can be modeled as [10]

$$T(h) = 288.15 - 0.00654h \quad (10)$$

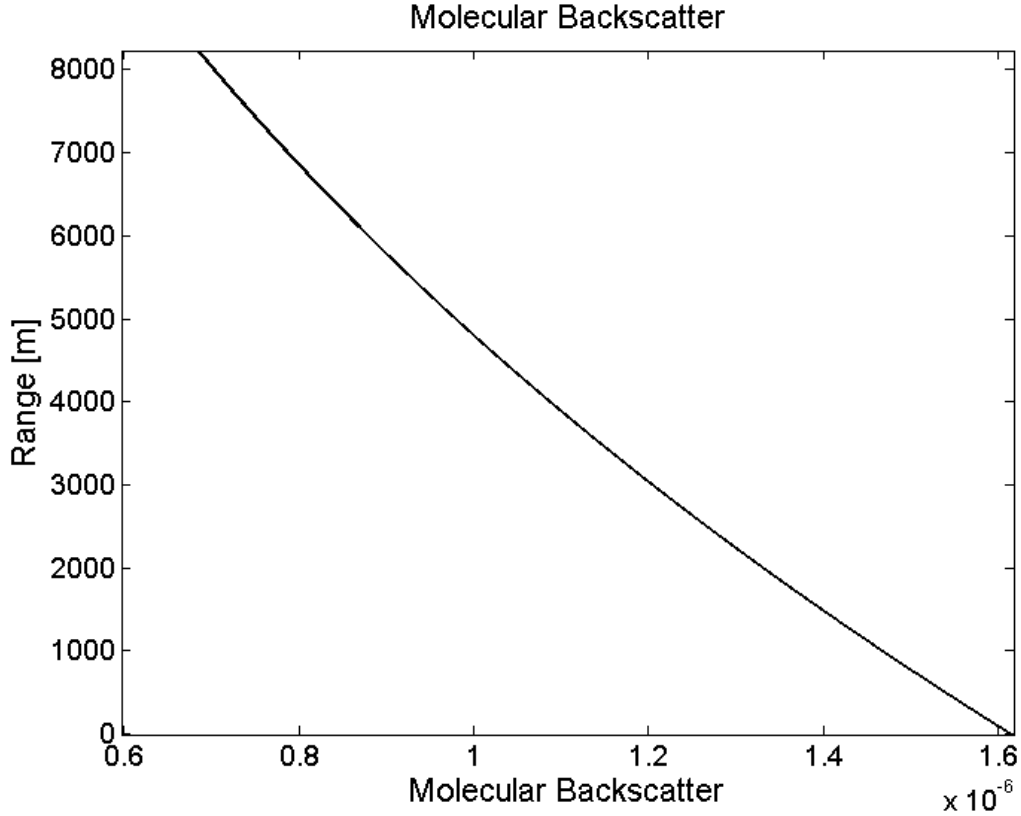


Figure 19: Range resolved, modeled molecular backscatter coefficient.

where h is the height above mean sea level given in meters and the temperature, $T(h)$, is given in Kelvin. The pressure over the same altitude range can be modeled as [10]

$$P(h) = 1.013 \times 10^5 \left[\frac{288.15}{T(h)} \right]^{-5.2199} \quad (11)$$

where the pressure, $P(h)$, is given in Pascals. The molecular backscatter coefficient can be computed from the temperature and pressure profiles using the following equation [10]

$$\beta_R(\lambda, r) = \frac{374.28 \left(\frac{P(h)}{T(h)} \right)}{\lambda^4} \quad (12)$$

where λ is given in nm and $\beta_R(\lambda, r)$ is given in (meter steradians) $^{-1}$. The extinction coefficient can then be found using $S_R(\lambda) = \frac{8\pi}{3}$.

Once the molecular and aerosol lidar returns have been found, aerosol backscatter and extinction coefficients are calculated. The basic lidar equation can be written in terms of its aerosol and molecular components,

$$P_{0,M}(r) = \frac{C_0\beta_M(r)T^2(r)}{r^2} \quad (13)$$

$$P_{0,A}(r) = \frac{C_0\beta_A(r)T^2(r)}{r^2}, \quad (14)$$

where β_A and β_M are the aerosol and molecular backscatter coefficients, T^2 is the round trip transmission to and from range r , and the constant term,

$$C_0 = \epsilon P_0 \frac{c\tau}{2} A\nu, \quad (15)$$

where ϵ represents the overlap between the receiver and the transmitted light, P_0 is the transmitted optical power, τ is the temporal extent of the outgoing laser pulse, A is the area of the receiver, and ν is the system efficiency including the transmission and reflectivity of optical elements and detector efficiency [16]. The overlap function, ϵ , is generally assumed to be unity over ranges where atmospheric optical properties are to be computed; however, in some cases an estimated or calculated overlap function, $\epsilon(r)$, is used. The roundtrip transmission,

$$T^2(r) = \frac{P_{0,M}(r)r^2}{C_0\beta_M(r)}, \quad (16)$$

can be calculated using the molecular return signal and molecular backscatter values, $\beta_M(r)$, which are estimated using a modeled (or measured) atmospheric temperature and pressure profile [16]. Aerosol backscatter can be calculated by dividing equation 8 by equation 7 and rearranging:

$$\beta_A(r) = \frac{P_{0,A}(r)\beta_M(r)}{P_{0,M}(r)}. \quad (17)$$

By rewriting the roundtrip transmission as

$$T^2(r) = e^{-2\int_0^r \sigma_A(r') + \sigma_M(r') dr'}, \quad (18)$$

the aerosol lidar return can be described by

$$P_{0,A}(r) = \frac{C_0 \beta_A(r) e^{-2 \int_0^r \sigma_A(r') + \sigma_M(r') dr'}}{r^2}, \quad (19)$$

where σ_A and σ_M are the aerosol and molecular extinction coefficients respectively. Equation 16 can be used to numerically estimate σ_A (r) by rewriting the aerosol lidar return as

$$P_{0,A}(r) = \frac{C_0 \beta_A(r) e^{-2 [\int_0^{r-\Delta r} \sigma_A(r') + \sigma_M(r') dr' + \sigma_M(r) \Delta r + \sigma_A(r) \Delta r]}}{r^2}, \quad (20)$$

which can be simplified to

$$P_{0,A}(r) = \frac{C_0 \beta_A(r) T^2(r - \Delta r) e^{-2(\sigma_A(r) \Delta r + \sigma_M(r) \Delta r)}}{r^2}, \quad (21)$$

Using equation 9 and a molecular extinction value calculated from a modeled atmospheric temperature and pressure profile [*9], the aerosol extinction coefficient,

$$\sigma_A(r) = \ln \left(\frac{P_{0,A}(r) r^2}{C_0 r \beta_A(r) T^2(r - \Delta r) \Delta r} \right), \quad (22)$$

can be calculated. This method for calculating S_A is susceptible to noise, and is impractical for use with noisy lidar signals. When excess noise is present, another approach is used which involves analyzing the aerosol transmission. The aerosol component of the round-trip transmission, $T^2(r)$, described by equation 16 is found by dividing out the modeled molecular transmission:

$$T_A^2(r) = \frac{T^2(r)}{T_M^2(r)} \quad (23)$$

The aerosol optical depth is computed by taking the natural logarithm of the of the aerosol transmission:

$$\tau_A(r) = -\frac{1}{2} \ln (T_A^2) \quad (24)$$

The aerosol optical depth is differentiated with respect to range to yield,

$$\sigma_A(r) = 2 \frac{\delta \tau_A(r)}{\delta r}, \quad (25)$$

the aerosol extinction coefficient. Another atmospheric optical property of interest, the aerosol lidar ratio S_A , is a ratio of the aerosol extinction and backscatter coefficients:

$$S_A(r) = \frac{\sigma_A(r)}{\beta_A(r)}. \quad (26)$$

The extinction to backscatter ratio is retrieved from the HSRL data without relying on the assumptions of a constant lidar ratio, or a boundary condition. $P_{A,0}(r)$, and $P_{M,0}(r)$ are retrieved from the transmitted and reflected lidar return signals. These are then used along with a molecular scattering model to calculate the aerosol backscatter, $\beta(r)$. Aerosol extinction, $\sigma_A(r)$, is calculated using the aerosol transmission, $T_A(r)$.

DATA

Initial data collected with the HSRL occurred at the Montana State University campus in Bozeman, Montana (45.68 N, 111.04 W, elevation 1468 m) during the months of January through May. Bozeman experiences a dry continental climate with an average August (January) high temperature of 28 C (1 C) with large diurnal temperature variability due to the high altitude and dry climate conditions. Bozeman is also characterized by low aerosol optical depths, typically less than 0.07 (at 532 nm) most days of the year. During observation periods with low aerosol optical depth, the lidar ratio typically clusters around either 50 sr or 100 sr while during periods of higher aerosol optical depth, the lidar ratio is variable depending on episodic events such as forest fires or agricultural activity that leads to increased aerosol loading.

The attenuated molecular backscatter return signal as a function of range is shown as the solid black line in figure 20 for data collected on January 16, 2012. The dashed blue line is a plot of the expected molecular backscatter as a function of range for the modeled molecular scattering, which does not take into account any contributions from aerosols. A plot of the aerosol attenuated backscatter is shown in figure 21. Most of the atmospheric aerosols were maintained within the planetary boundary layer (PBL) located at a height of approximately 1.1 km while broken clouds were present near 5 km. The aerosol optical depth observed by the co-located AERONET site was 0.052. Using the HSRL inversion technique described above, the retrieved aerosol backscatter and aerosol lidar ratio profiles are shown in figures 22 and 23 respectively. Additionally, the lidar ratio as calculated from AERONET data is presented in figure 23, alongside the HSRL retrieved S_A . The lidar data used to calculate the S_A were collected at 17:48 UTC, while the AERONET data used in the inversion were collected at 18:37 UTC, with no major meteorological events occurring

in the interim.

The aerosol lidar ratio can be calculated from AERONET retrieved data as

$$S_A = \frac{4\pi\omega_0}{P(\Theta = 180^\circ)}. \quad (27)$$

where Θ_0 is the retrieved single scatter albedo and $P(\Theta = 180)$ is the retrieved scattering phase function at $\Theta = 180$. For the AERONET retrieved $\Theta_0 = 0.807$ and $P(\Theta = 180) = 0.101$, the retrieved column averaged lidar ratio was $S_A = 100.3$ sr. This high lidar ratio has been observed during other periods of relatively low aerosol optical depth over Bozeman and is most sensitive to changes in the imaginary part of the index of refraction [29]. In this case, wood burning and other urban sources may be contributing both more absorptive and larger particles trapped within the low planetary boundary layer, causing a relatively high S_A value. The dashed vertical line shown in figure 23 represents the column average lidar ratio retrieved from a co-located aerosol robotic network (AERONET) site. Good agreement between the column average lidar ratio retrieved from the AERONET data and lidar ratio retrieved from the HSRL is seen in this figure.

The attenuated molecular and aerosol backscatter return signals are shown in figures 24, and 25 for data collected on February 6, 2012. The solid black line in the left hand figure represents the attenuated molecular backscatter signal while the dashed blue line represents the modeled molecular backscatter. The majority of the atmospheric aerosols are contained below approximately 2 km with a thin enhanced aerosol layer forming near the top of the PBL. A cloud is present at 6 km producing the large return seen at that height in the right hand plot. Because clouds were present on this day, the solar radiometer was not able to collect data. However, the aerosol optical depth can be estimated using the measured attenuated molecular backscatter signal. The total round trip transmission is equal to the ratio of the

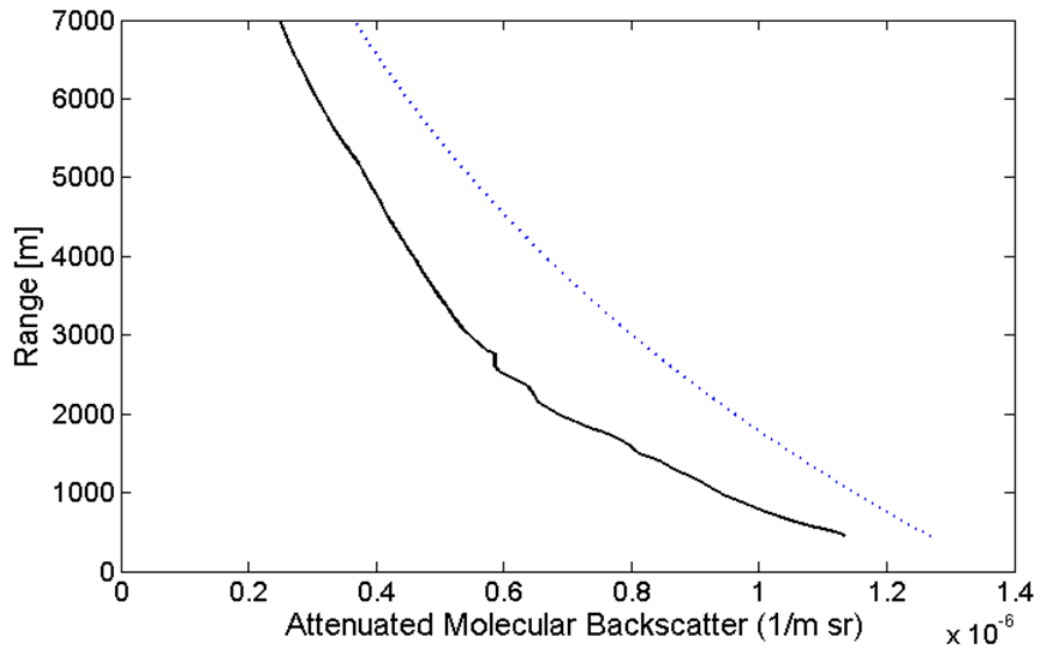


Figure 20: A plot of the attenuated molecular backscatter as a function of range is shown as the solid black line. The modeled molecular backscatter is shown as the dotted blue line in this figure.

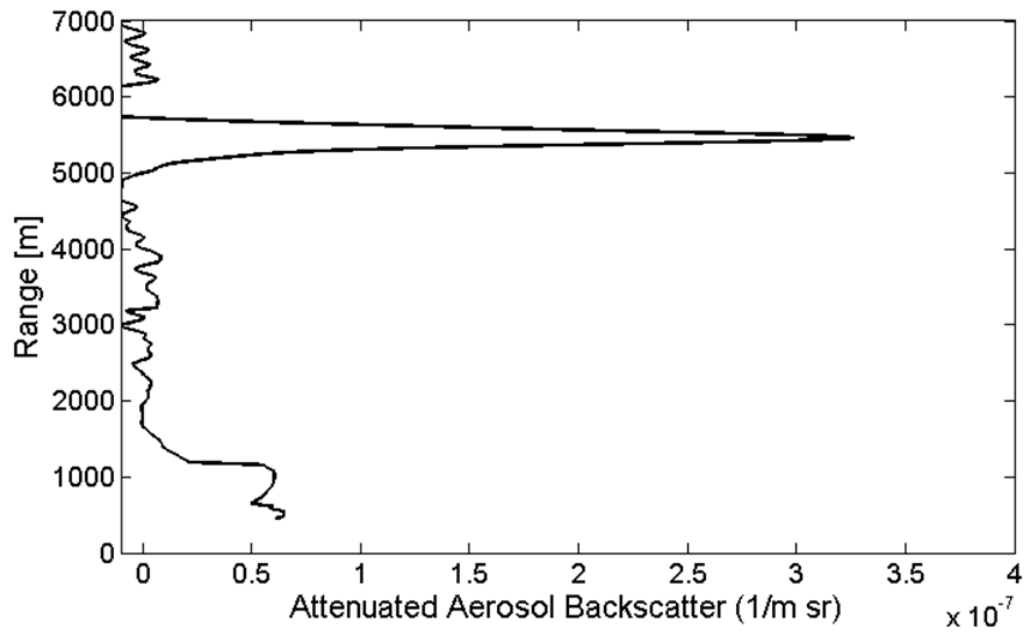


Figure 21: A plot of the attenuated aerosol backscatter as a function of range. The aerosols are mostly confined below the planetary boundary layer at approximately 1.1 km.

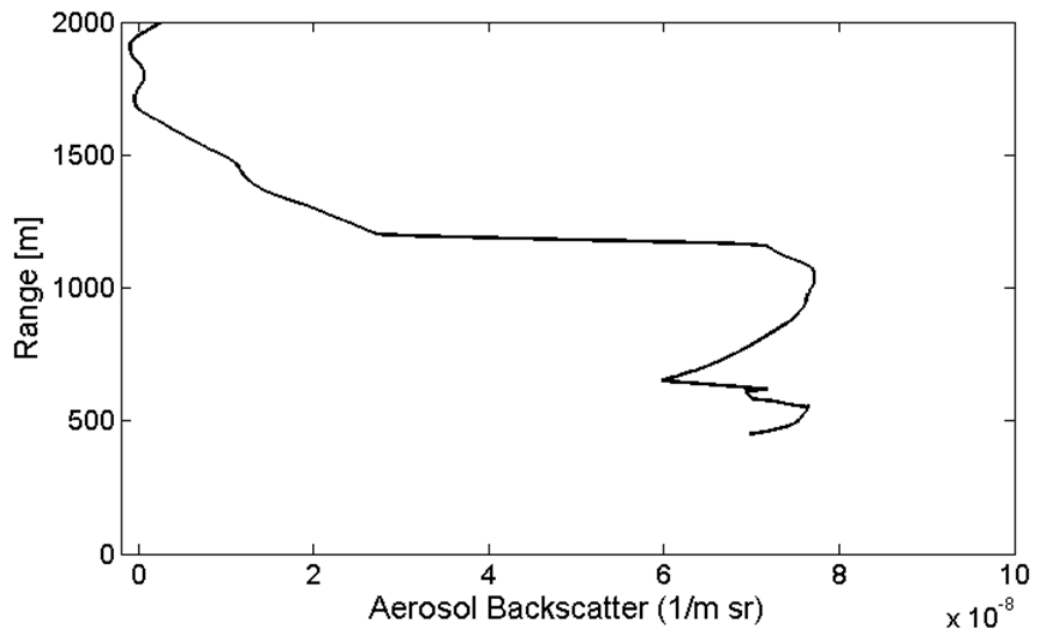


Figure 22: The aerosol backscatter as a function of range calculated by scaling the modeled molecular backscatter by the ratio of the measured aerosol and molecular return signals shown in figures 8 and 9.

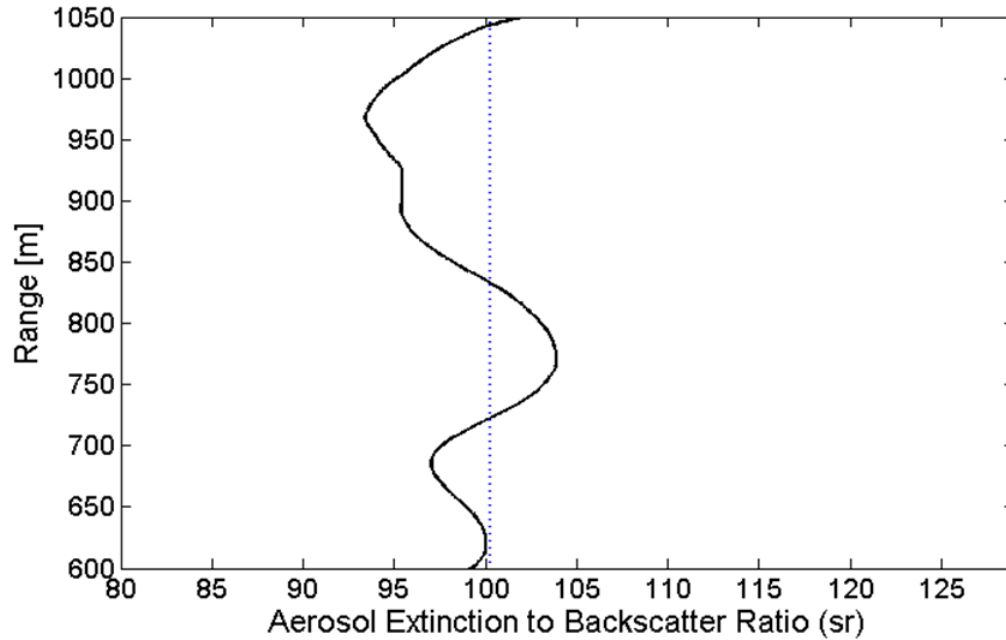


Figure 23: The lidar ratio as a function of range retrieved from the aerosol and molecular signals shown in figures 8 and 9 is plotted as the solid line. The lidar ratio is plotted from 600 m where the HSRL comes into full overlap to the planetary boundary layer at 1.1 km. The vertical line represents the column averaged lidar ratio calculated from the inverted AERONET data. The lidar data used to calculate the SA were collected at 17:48 UTC, while the AERONET data used in the inversion was collected at 18:37 UTC.

measured attenuated molecular backscatter to the modeled molecular backscatter. Using data above the PBL but below the cloud, the ratio of the measured attenuated molecular backscatter to the modeled molecular backscatter is 0.79 at 5 km. The estimated round trip transmission from the molecular model at 5 km is 0.90. Thus the round trip aerosol transmission is (5 km) = $.79/.90 = 0.88$. For this round trip aerosol transmission, the corresponding aerosol optical depth is 0.065. A plot of the HSRL retrieved aerosol extinction as a function of range is shown in figure 27 while the corresponding retrieved lidar ratio as a function of range is shown in figure 27. The column averaged lidar ratio through 1.4 km is $S_A = 49$ sr, which matches that of the Cattrall et al. derived rural continental aerosol grouping [30, 31]. This rural continental aerosol model has been found to sometimes be representative of aerosols over Bozeman, Montana during periods of low aerosol optical depth, although, as already noted, low optical depth situations can also yield high S_A values as was the case for the January 16, 2012 observations [29, 31].

Figures 28 through 32 show a thin, low layer of clouds moving over Bozeman on the morning of February 28th, 2012. The S_A value of approximately 30 retrieved from these data is consistent with that expected for cumulus clouds [32, 33]. Figures 31 and 32 demonstrate the ability of the HSRL instrument to maintain stable operation long enough to provide time-series data and retrieved aerosol optical properties.

Figures 33 - 35 show a layer of aerosols near the ground on March 10th. A co-located micro-pulsed lidar operating at 532 nm measured a column averaged S_A of 120, which strongly agrees with the retrieved S_A from the hsrl, shown in figure 33. These data were collected on a clear day, and the aerosols were concentrated near the ground. As previously discussed, the retrieved S_A is consistent with that found regularly on clear, clean days in Bozeman, MT [29, 31].

Figures 36 through 41 show data collected on Monday, May 7th, a clear but slightly

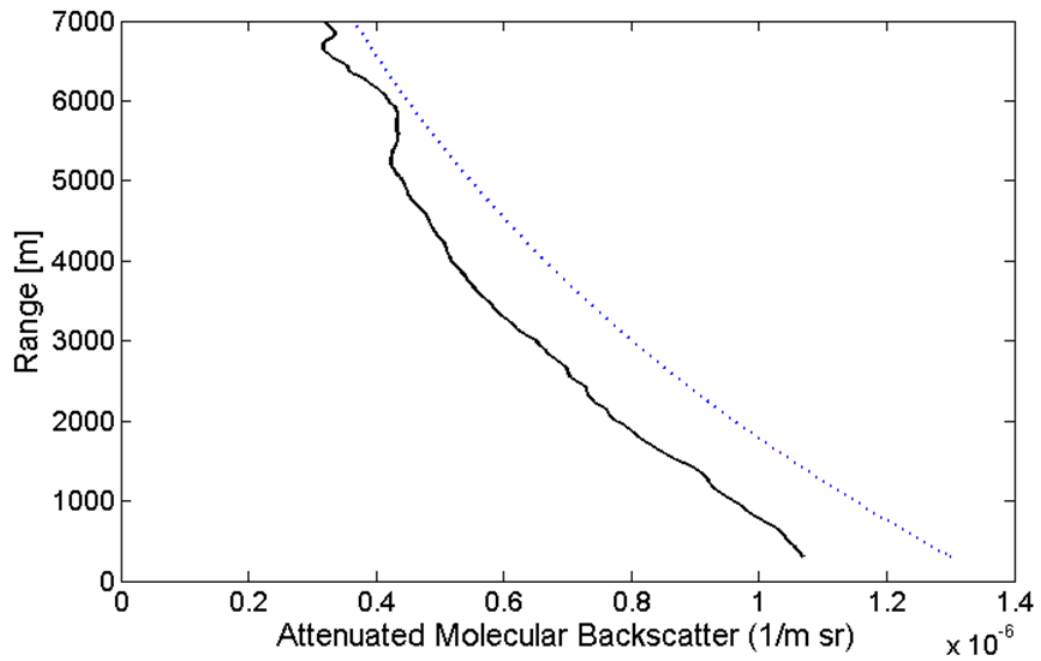


Figure 24: A plot of the attenuated molecular backscatter as a function of range is shown as the solid black line. The modeled molecular backscatter is shown as the dotted blue line in this figure.

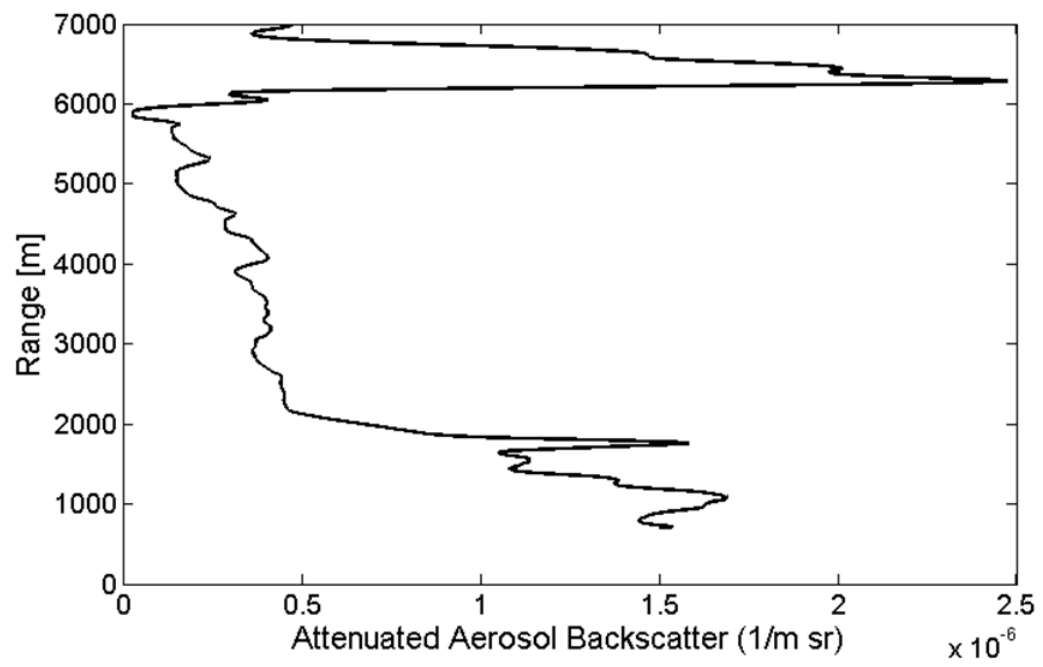


Figure 25: A plot of the attenuated aerosol backscatter as a function of range.

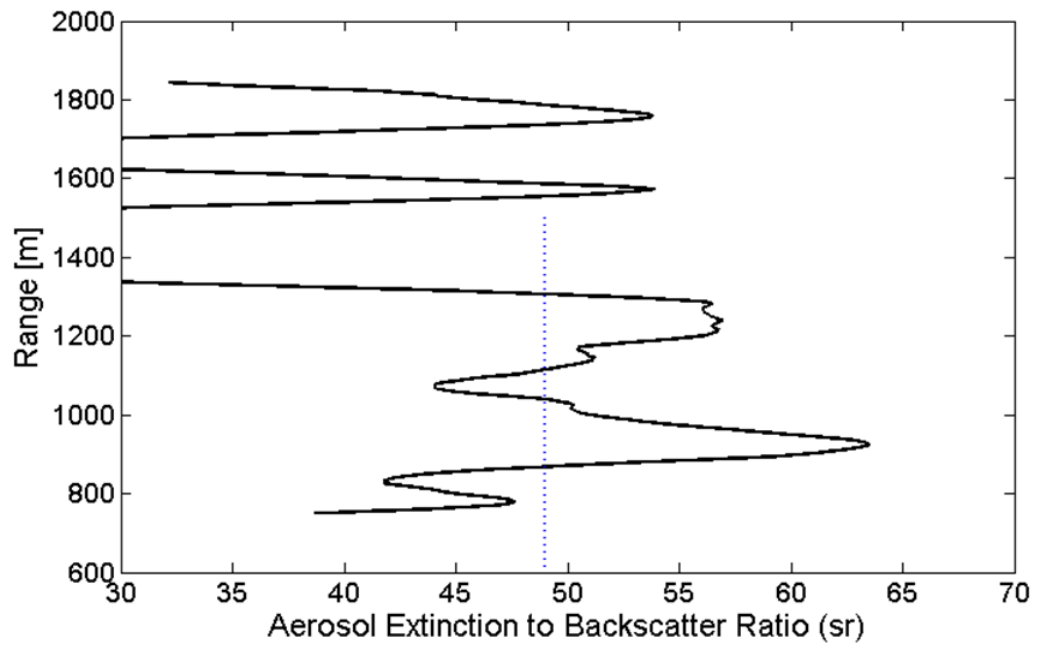


Figure 26: A plot of the retrieved S_A . The mean S_A within the planetary boundary layer is represented by the dotted line.

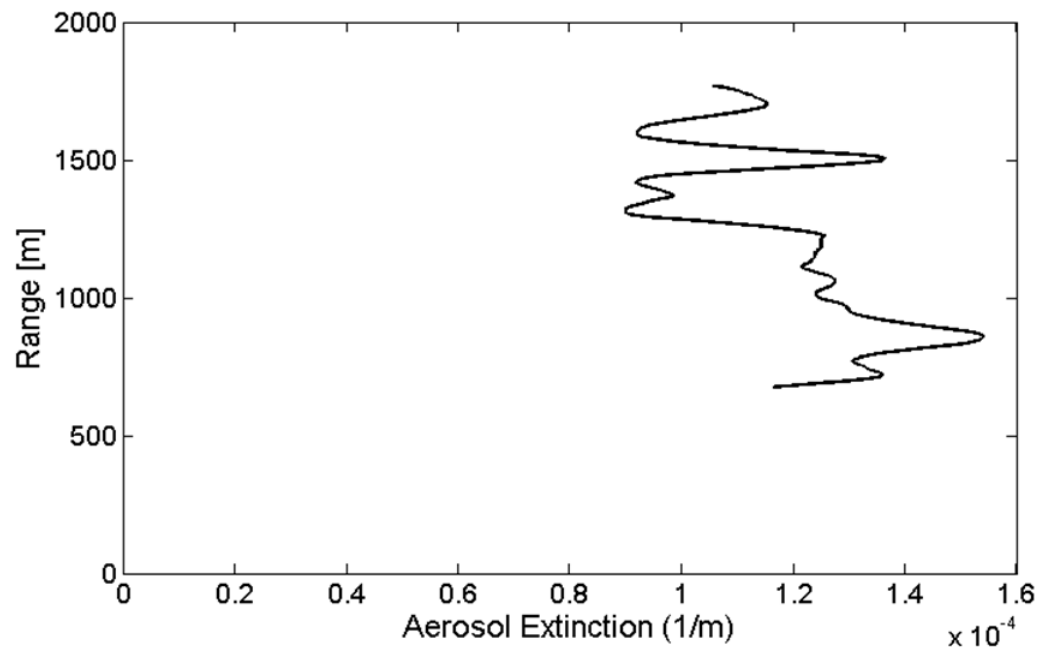


Figure 27: A plot of the aerosol extinction as a function of range. The aerosols are mostly contained below the planetary boundary layer at approximately 1.6 km with an aerosol layer forming near the boundary layer.

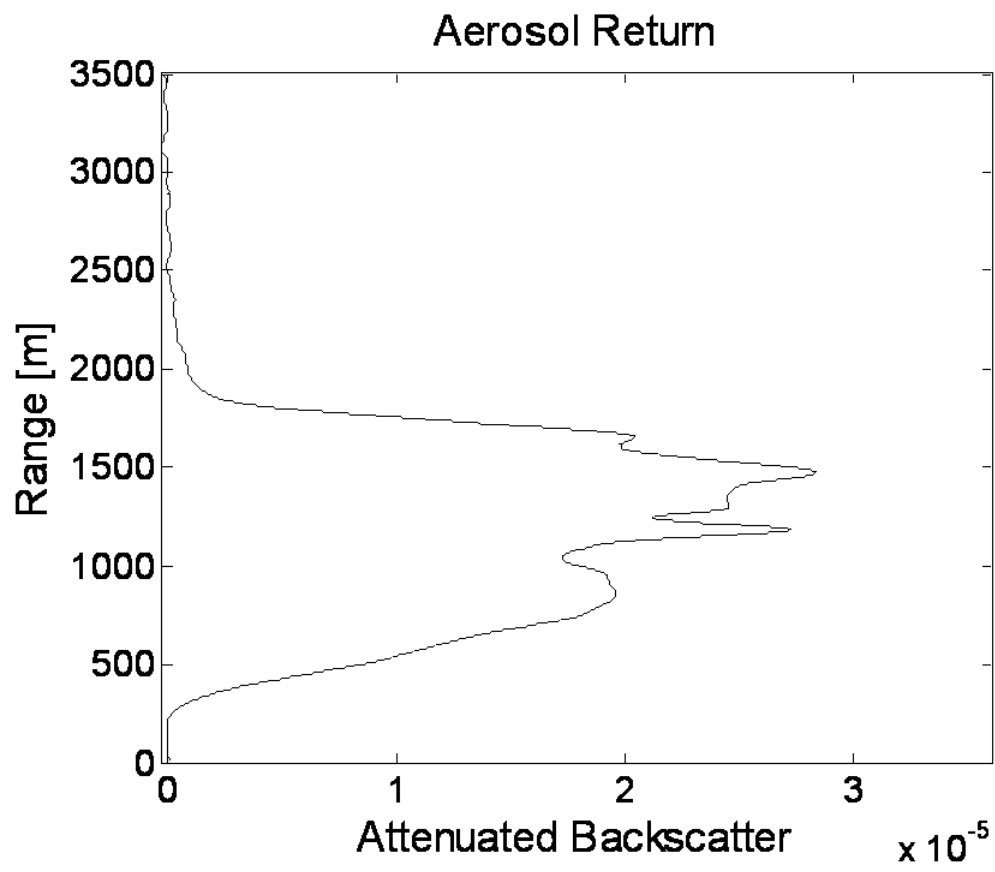


Figure 28: A plot of the aerosol attenuated backscatter as a function of range.

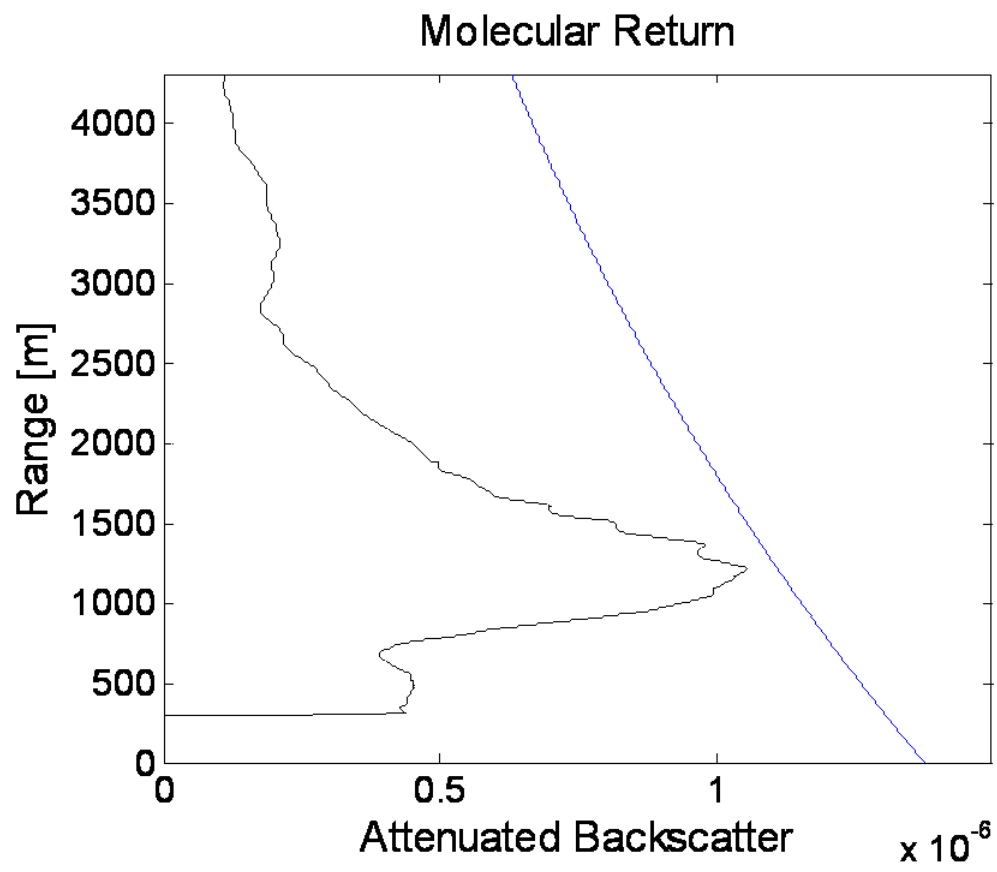


Figure 29: A plot of the molecular attenuated backscatter as a function of range.

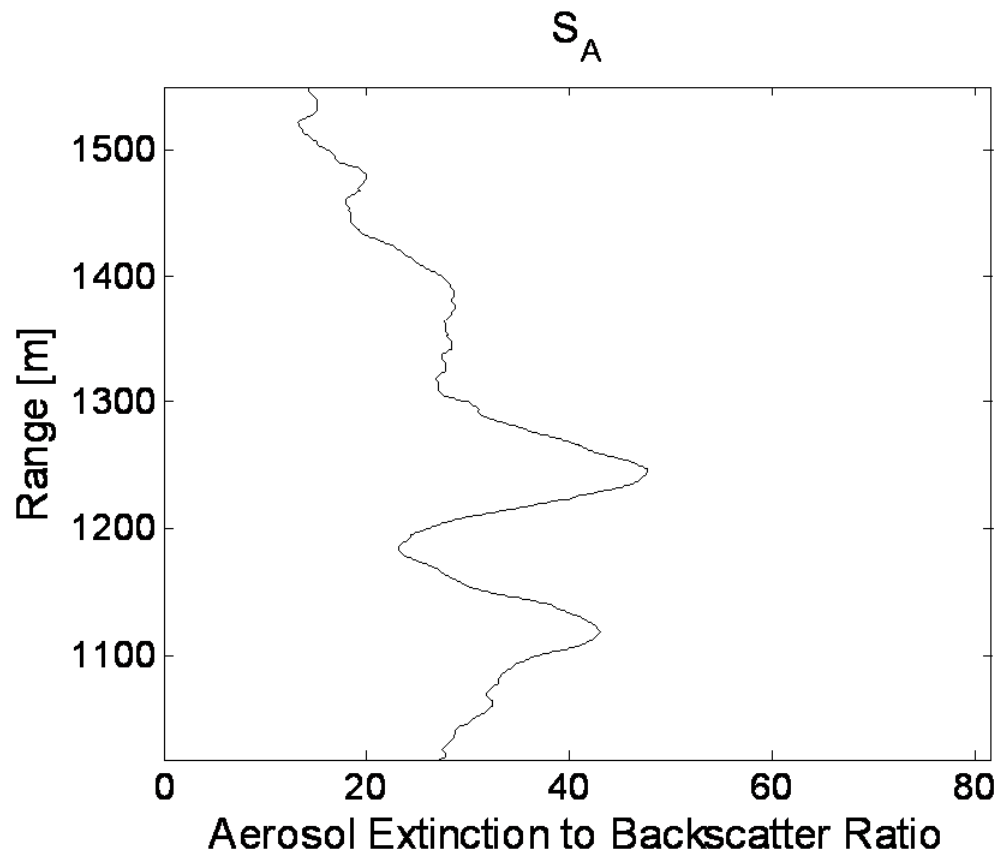


Figure 30: A plot of the aerosol extinction to backscatter as a function of range.

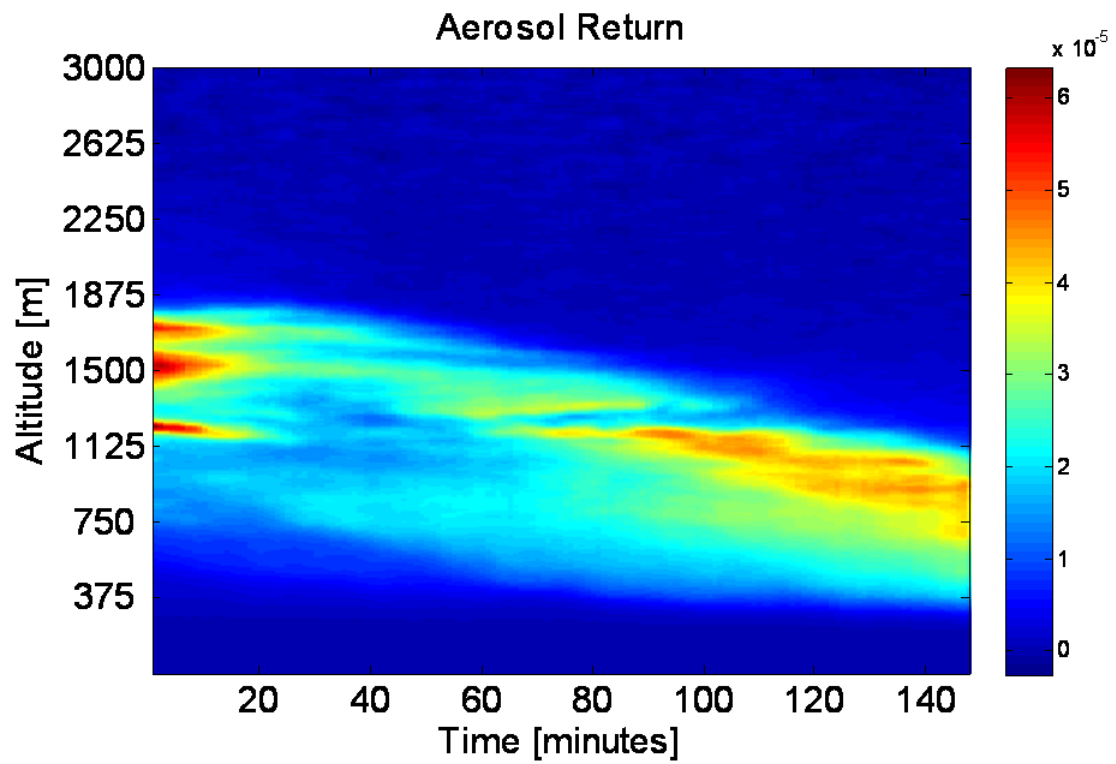


Figure 31: A plot of the aerosol attenuated backscatter as a function of range.

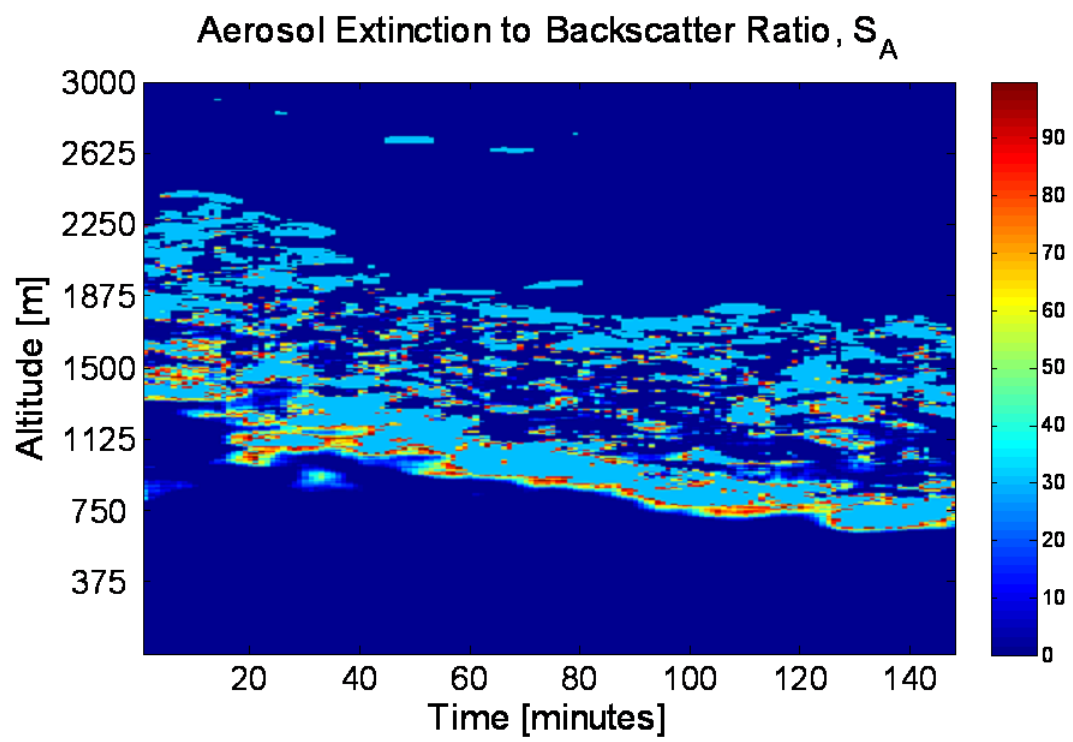


Figure 32: A plot of the aerosol extinction to backscatter ratio as a function of range.

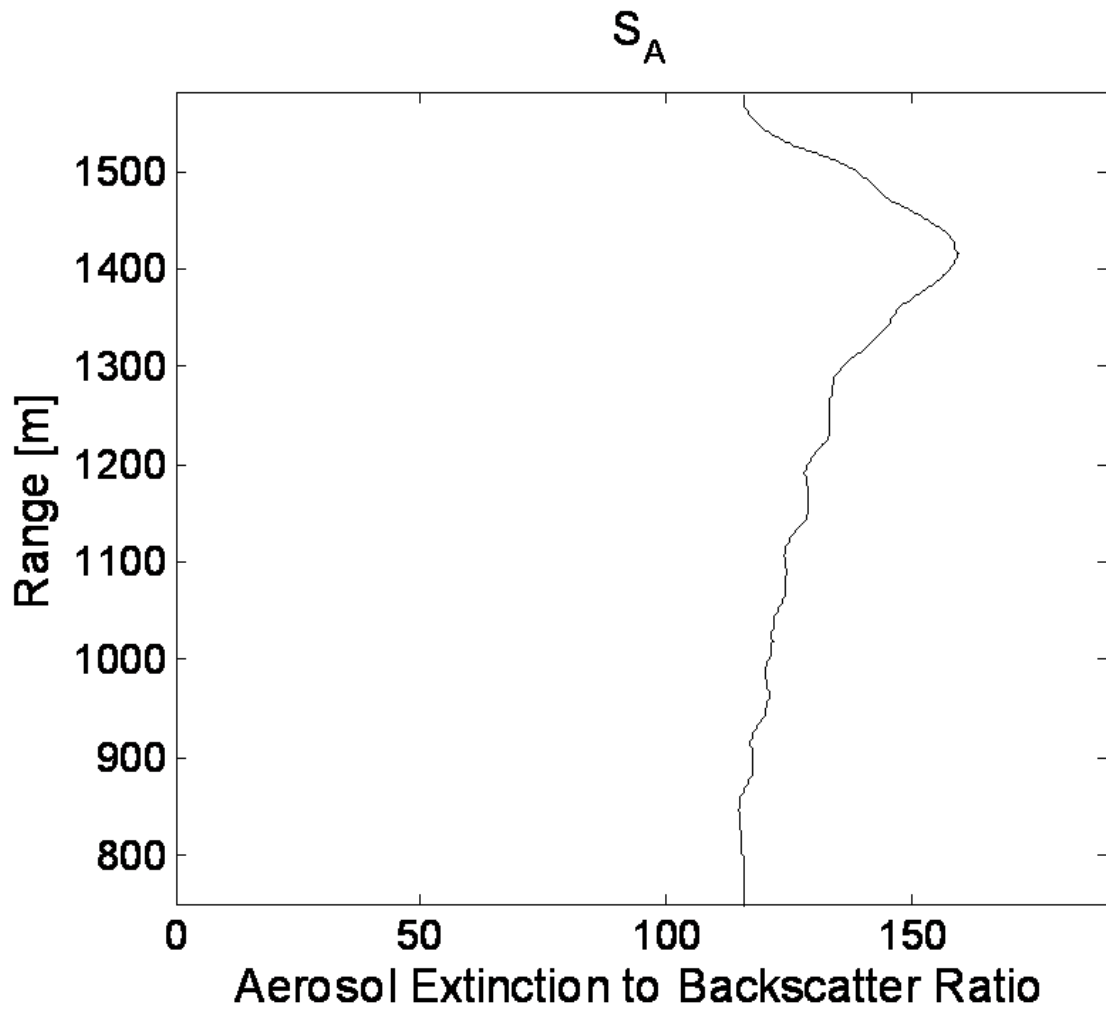


Figure 33: A plot of the aerosol extinction to backscatter ratio as a function of range.

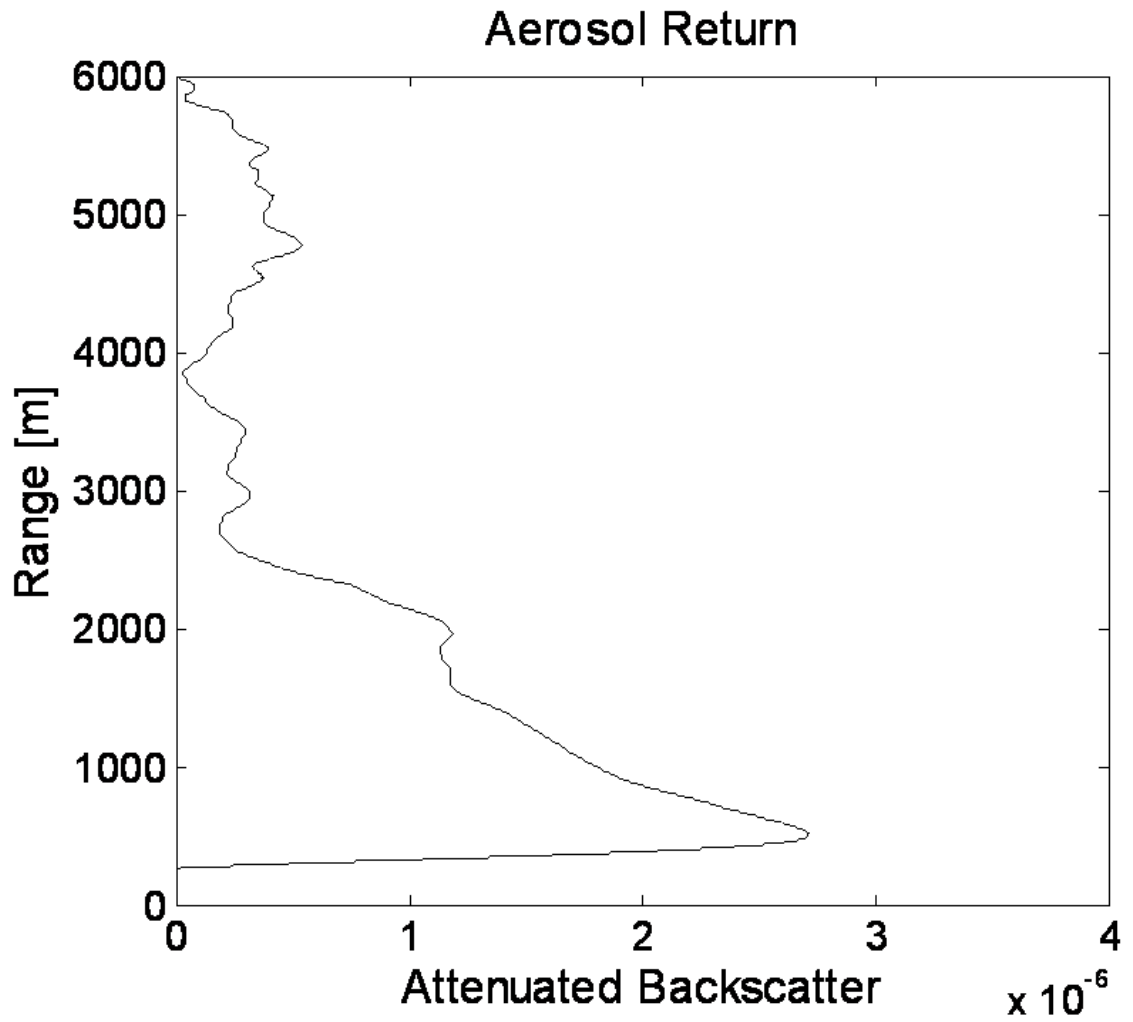


Figure 34: A plot of the aerosol extinction to backscatter ratio as a function of range.

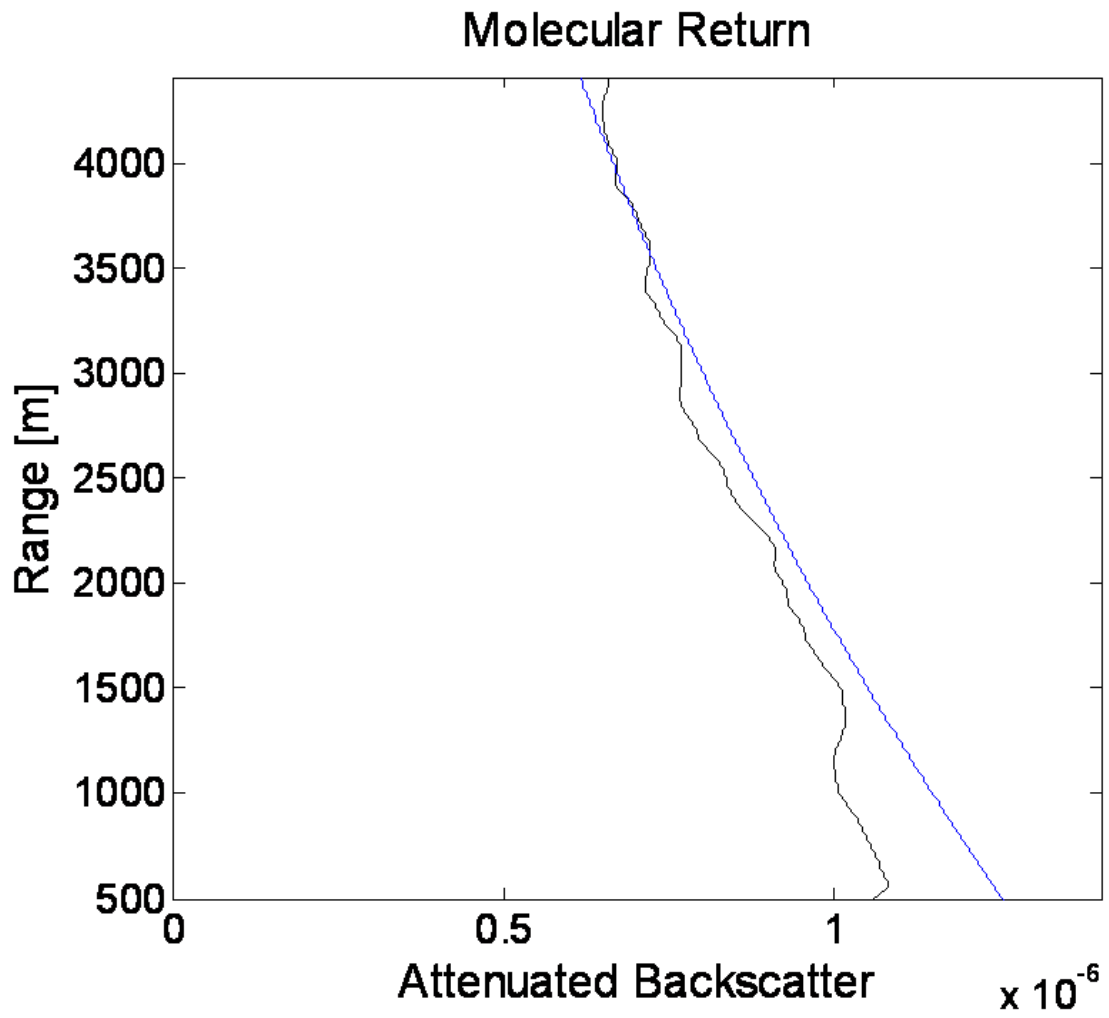


Figure 35: A plot of the aerosol extinction to backscatter ratio as a function of range.

hazy day. The data show a well defined aerosol layer within the PBL, with a slightly higher concentration of aerosols at the top of this layer. An S_A of approximately 50 was retrieved for this upper enhanced layer, while an S_A of 30 was retrieved for the lower portion of the layer. The thin upper layer, with a higher S_A , may be a mixture of the lower aerosol layer and smoke from prescribed burns being carried out on a nearby mountain upwind of the data collection site. Figures 40 and 41 show time series plots of the aerosol return and S_A retrieved from the May 7th data.

The data and retrieved atmospheric parameters presented in this chapter demonstrate that the HSRL instrument is working properly. The data and atmospheric parameters correlate well with data from co-located instruments, and are consistent with previous atmospheric studies carried out near Bozeman, MT.

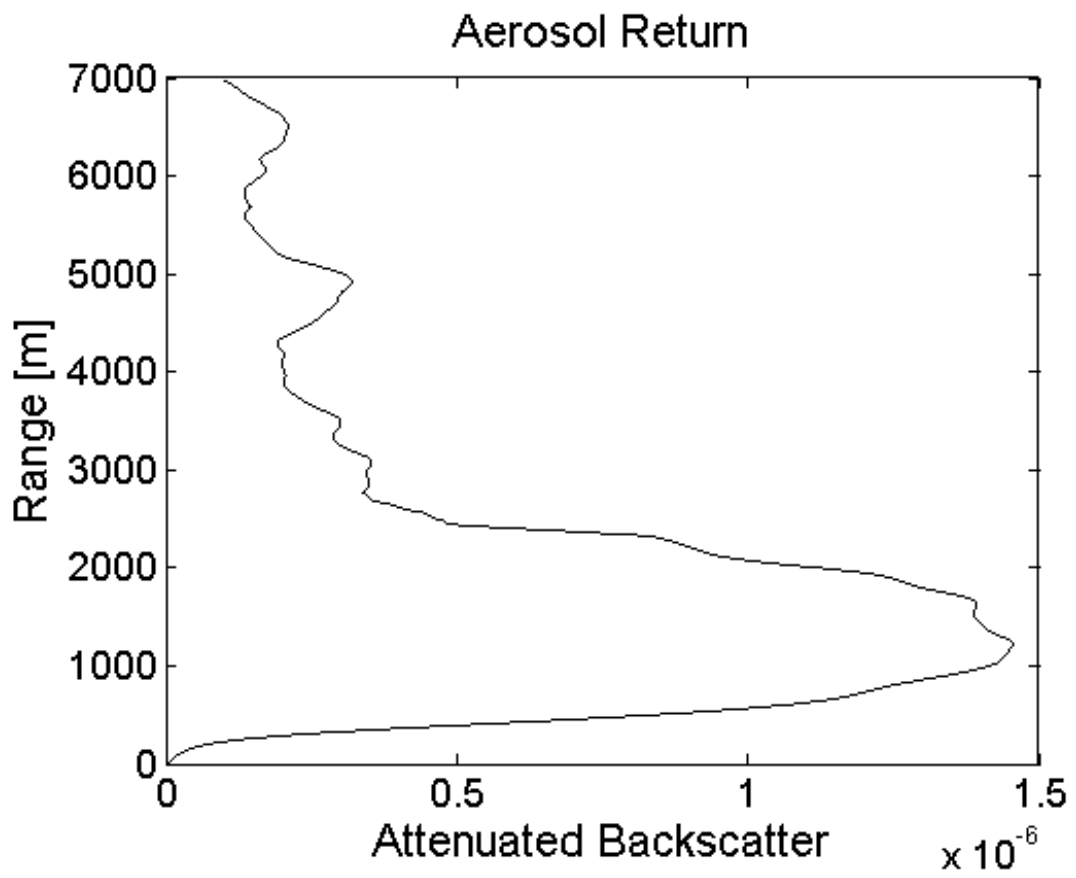


Figure 36: A plot of the retrieved aerosol lidar return for May 7th.

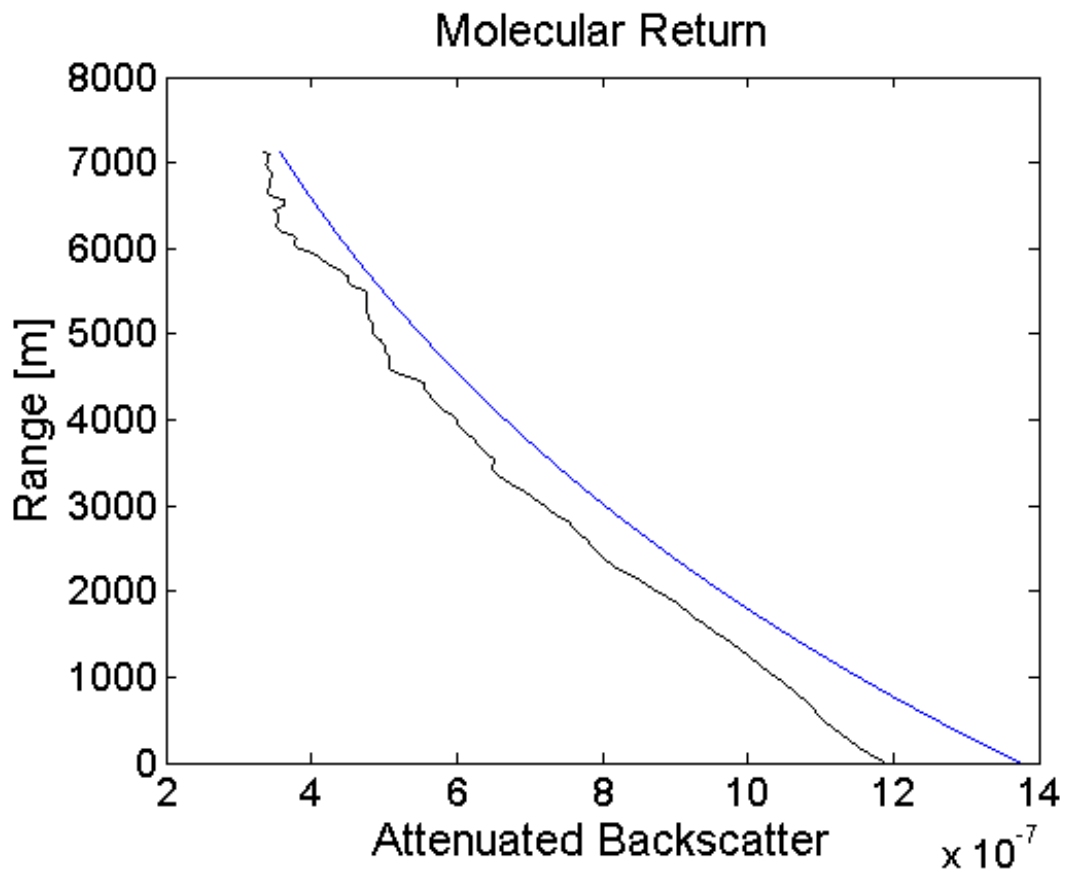


Figure 37: A plot of the retrieved molecular lidar return for May 7th. The blue line represents a modeled molecular return with no aerosol contribution.

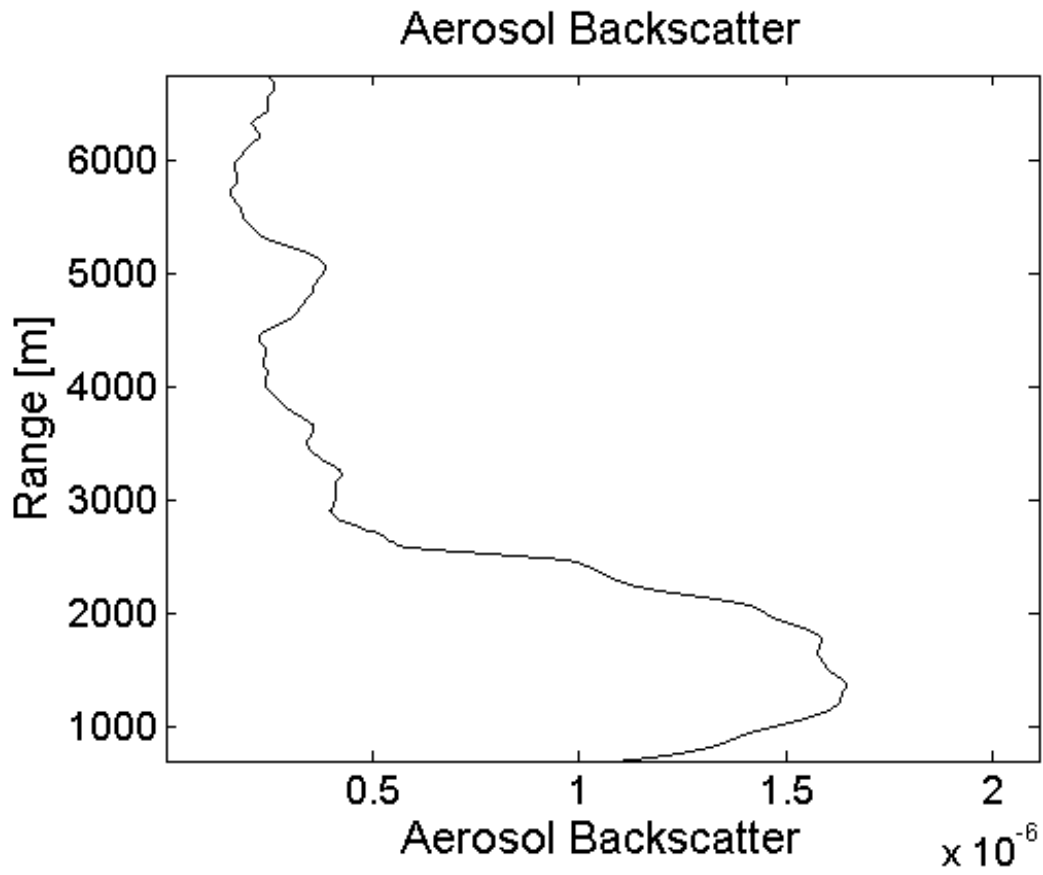


Figure 38: A plot of the retrieved aerosol backscatter coefficient as a function of range for May 7th.

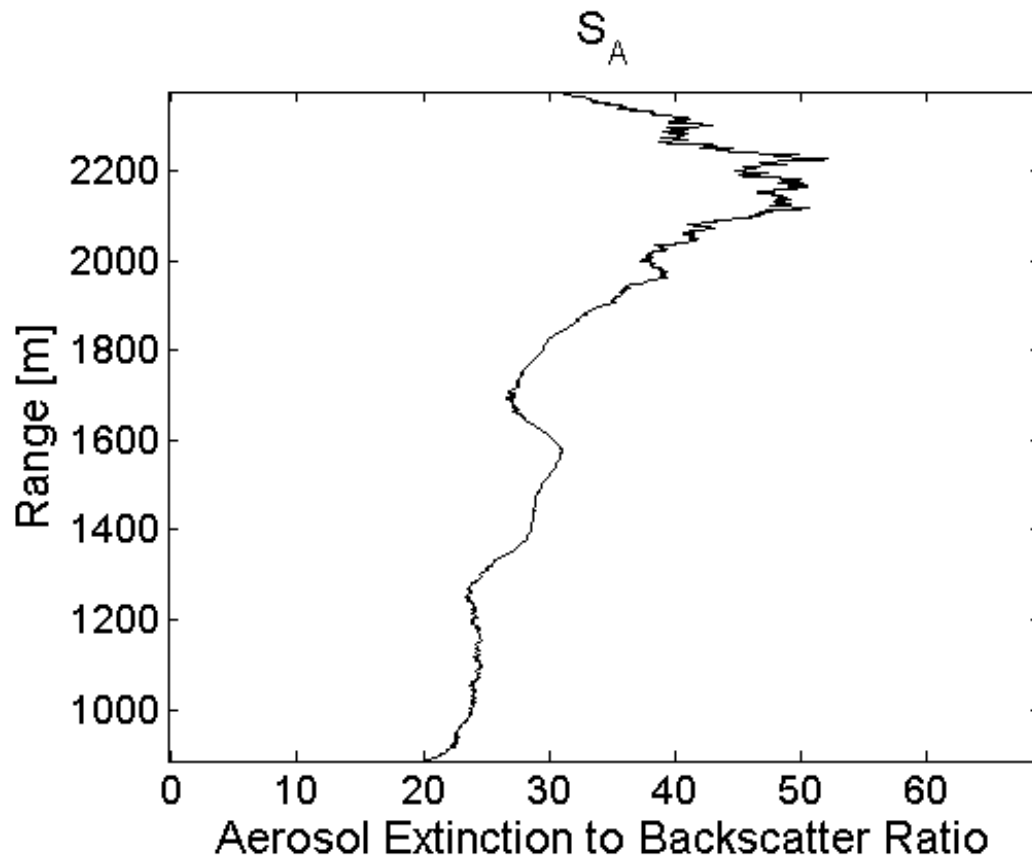


Figure 39: A plot of the aerosol extinction to backscatter ratio as a function of range for May 7th.

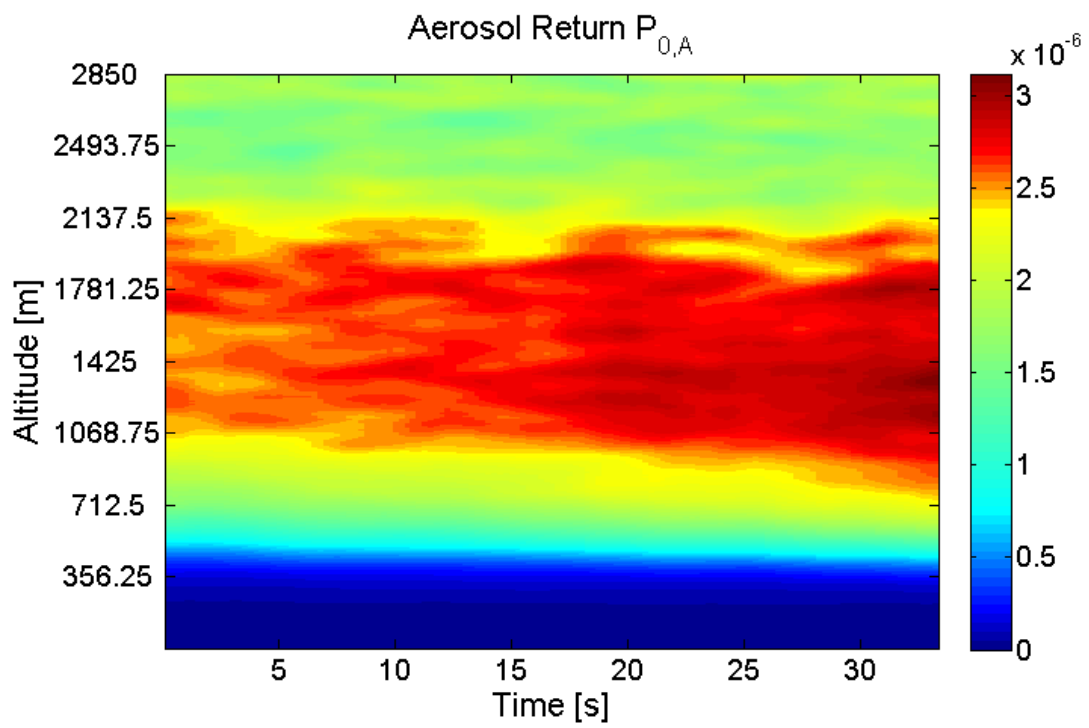


Figure 40: A time-series plot of the retrieved aerosol return for May 7th.

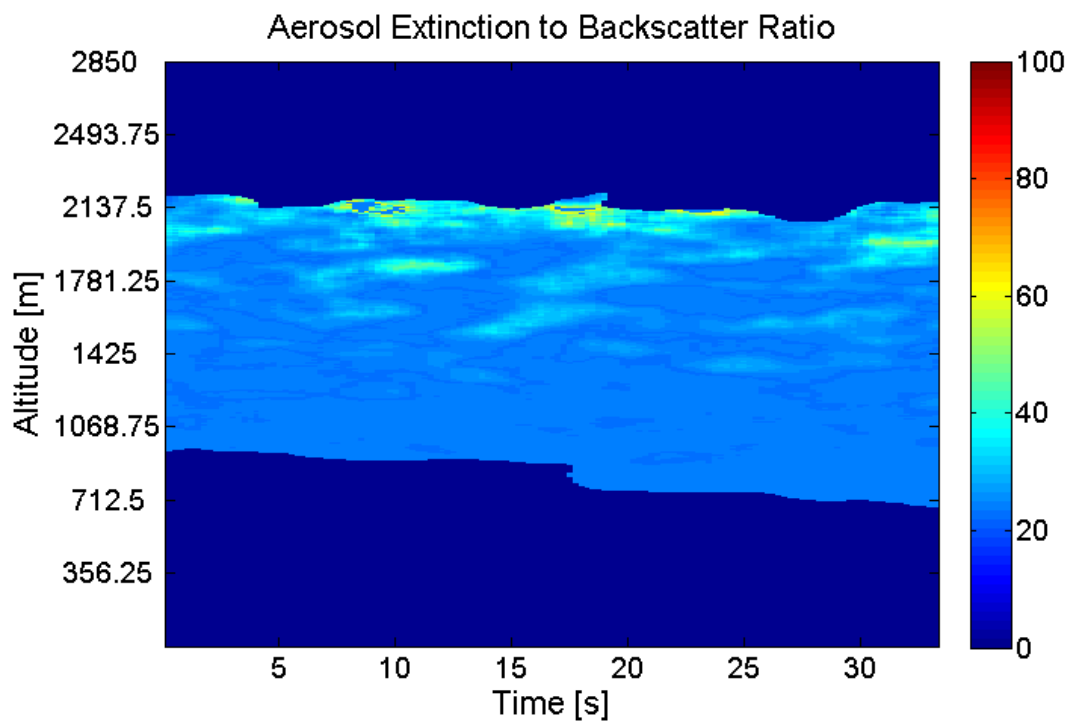


Figure 41: A time-series plot of the aerosol extinction to backscatter ratio as a function of range for May 7th.

ERROR ANALYSIS

Detector Signal to Noise Calculations

Error in the lidar instrument comes primarily from three sources: noise from the photomultiplier tubes, error in retrieval of the molecular and aerosol signals due to uncertainties in the CFP transmission, and error introduced through the digitization and numerical processing of the data. Detector noise is a significant source of error in data produced by the HSRL instrument, and can have a significant impact on retrieved atmospheric parameters. This detector noise introduced by the PMTs used in the HSRL instrument can be expressed as [34],

$$Noise_{PMT}(r) = \sqrt{4eBG \left(\frac{1}{1 - \frac{1}{\delta}} \right) I(r) + 4eBI_{dark} + \frac{4kTB}{R_L}}, \quad (28)$$

where e is the charge of an electron, B is the bandwidth of the PMT, G is the overall gain of the PMT, δ is the gain of an individual dynode stage of the PMT, I_{dark} is the dark current of the PMT (at the anode), k is Boltzmann's constant, T is the temperature in Kelvin and R_L is the load resistance. Using manufacturer specified values of $\delta = 4$, $B = 714$ MHz, $G = 2 \times 10^6$, and $I_{dark} = 0.1$ nA, and a PMT output current of 2 mA (consistent with lidar returns from within the aerosol-rich planetary boundary layer), detector noise was calculated to be $226 \mu A$, which is 11% of the detected signal. A plot of the impact of detector noise on aerosol extinction to backscatter ratio retrieval is shown in figure 42. The noise level in the detected signal results in a greater than 40% error in the retrieved S_A , rendering a retrieval attempted with this raw data essentially useless. However, by averaging multiple lidar returns together, some of the noise introduced by the detectors can be removed. By applying a ten-point averaging filter across lidar returns -such that the same range-bin from

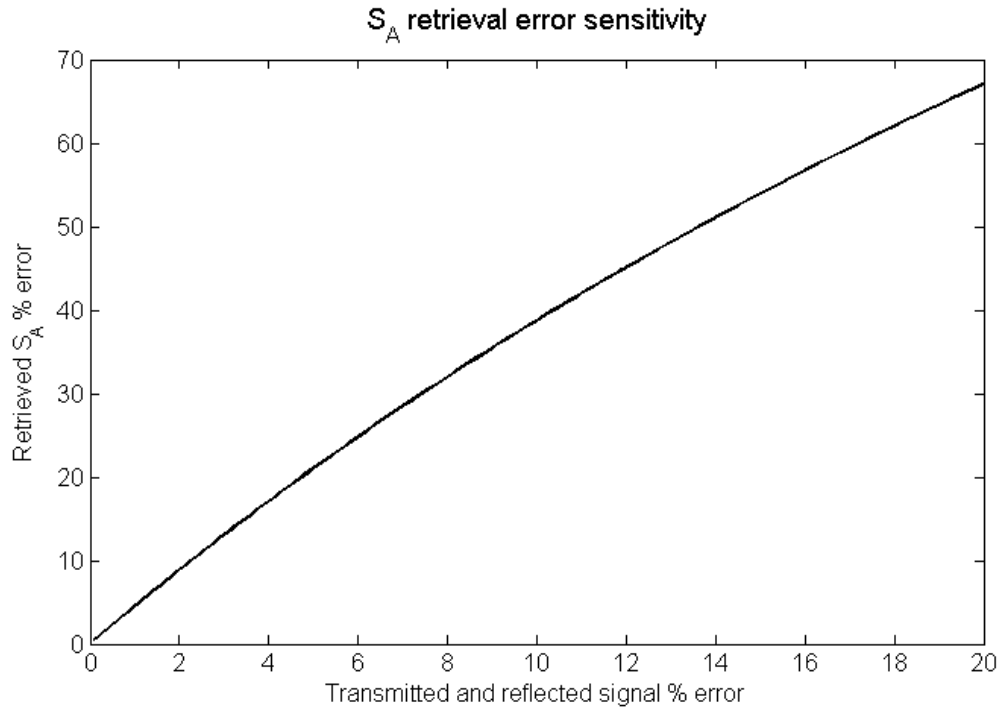


Figure 42: The worst case effects of detector error on S_A retrieval.

multiple returns are averaged together -the detector error is reduced by 51%. The efficacy of averaging lidar returns in this manner is highly dependant on the rate of change of atmospheric conditions. If the rate of change of the atmosphere is low, a large number of returns can be averaged together resulting in a significant noise reduction. However, if the rate of change of the atmosphere is high, averaging large numbers of returns together can filter out the desired signal in addition to noise, resulting in a distorted signal.

To illustrate this effect, figure 43 represents a series of lidar returns sampled at the same range bin (with a signal level consistent with a return from the PBL), changing at a rate of 8% per minute, while figure 44 shows the frequency response of a 10-point averaging filter. Most of the information contained in the series of lidar returns (figure 43) is low frequency because the returns are not changing very fast at a given

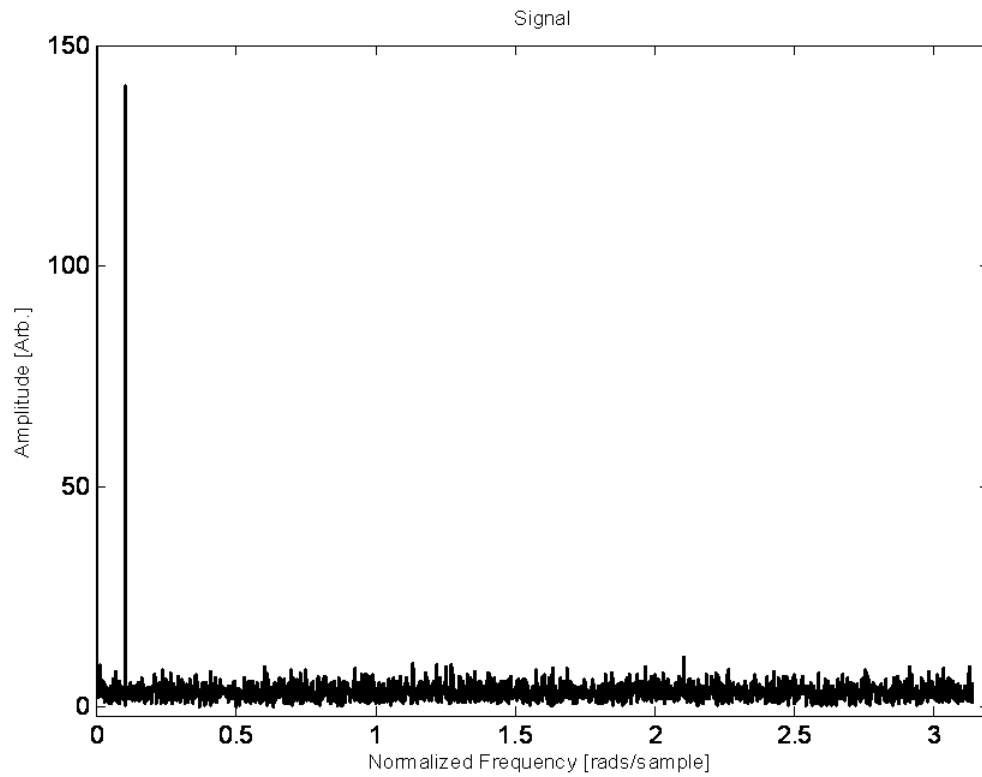


Figure 43: A modeled time-series of lidar returns observed at a single range bin in the frequency domain. The single low frequency spike represents the high-frequency limit expected in real data.

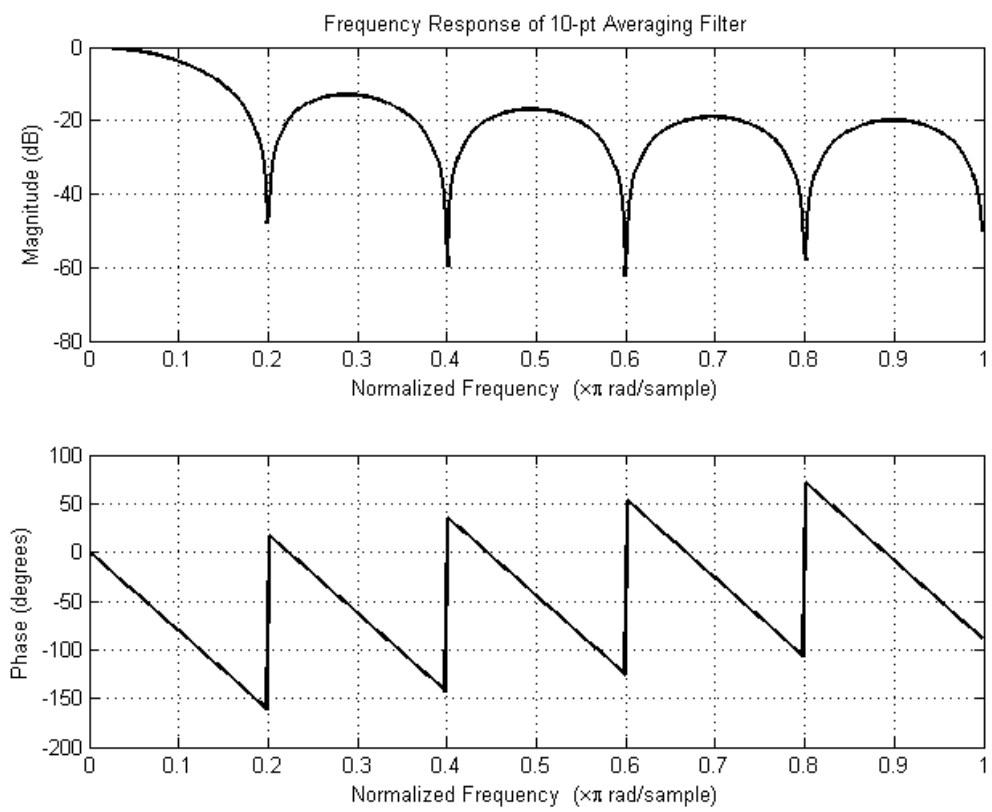


Figure 44: The frequency response of a 10-point averaging filter.

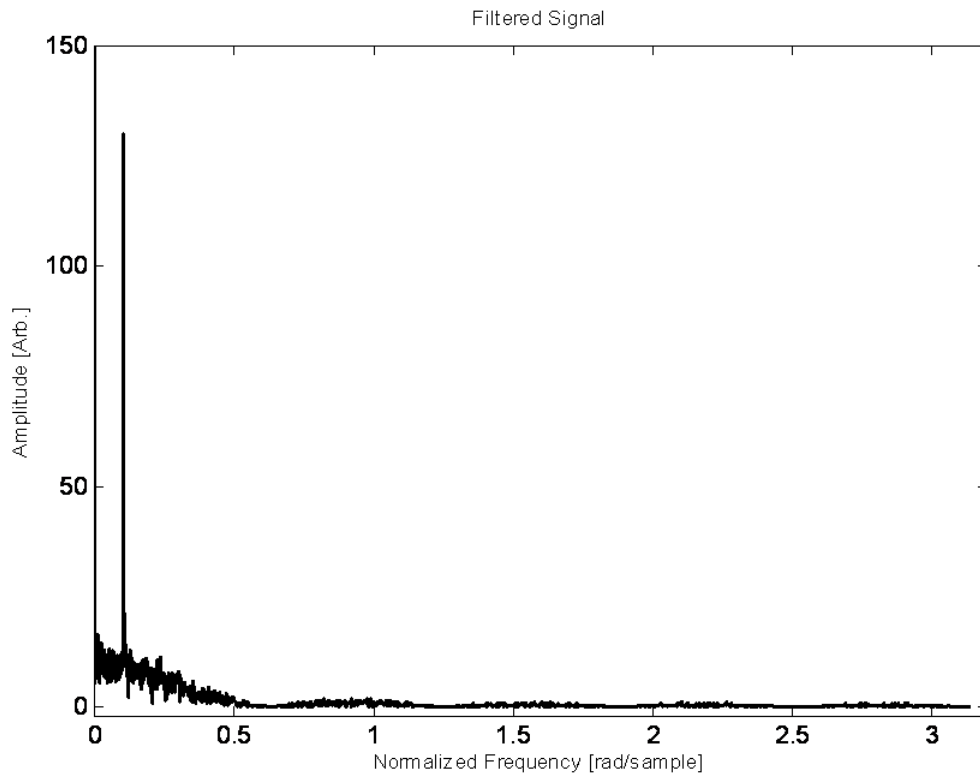


Figure 45: A modeled time-series of lidar returns observed at a single range bin in the frequency domain, after a filter has been applied to reduce the noise-content.

range bin. The uniformly distributed detector noise, however, is present throughout the spectrum. Much of this detector noise can therefore be removed from the signal via a low pass filter. Figure 45 shows the results of applying the 10-point averaging filter to the modeled data shown in figure 43.

Applying a multipoint averaging filter to individual lidar returns in the "range" dimension can also significantly reduce the level of the detector noise present in the signal. Figure 46 shows a modeled lidar return signal, while figure 47 shows that same signal after the application of a 30-range-bin averaging filter. The frequency response of this filter is shown in figure 48. The noise level has been reduced by 68%

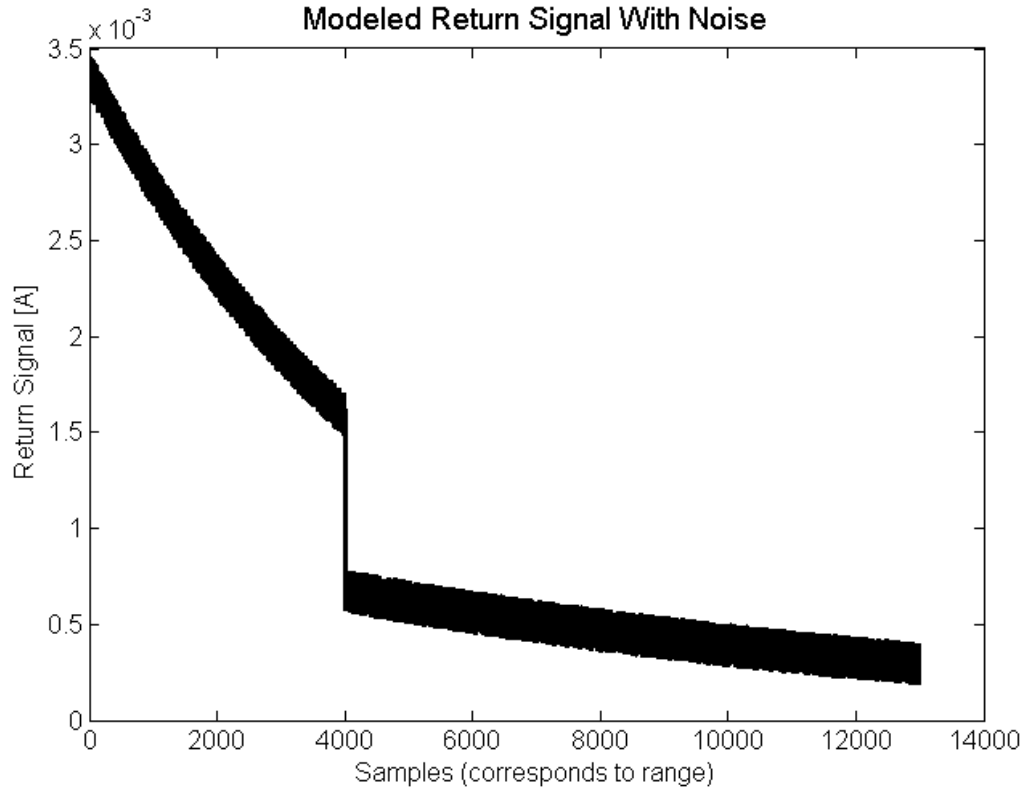


Figure 46: A modeled lidar return with a noise level constant with that produced by the PMTs in the HSRL.

through the use of this filter. By averaging the return signals in range and in time across multiple returns, the detector noise level has been reduced by 84%, to 1.7 % detector error. This filtering reduces the error in the retrieved S_A from 40% to 7.5%, allowing for meaningful retrieval of aerosol optical properties such as S_A .

Error and uncertainties in the CFP characterization are another potential source of error in the retrieval of S_A . The effect of K-value error on S_A is shown in figure 42. Error in the K-values comes from two sources: measurements of cavity transmission, and altitude resolved atmospheric models of temperature and pressure. The measurements of cavity transmission have a 3 – 5% standard deviation. The error of these measurements falls near or below 1% when 10 such measurements are

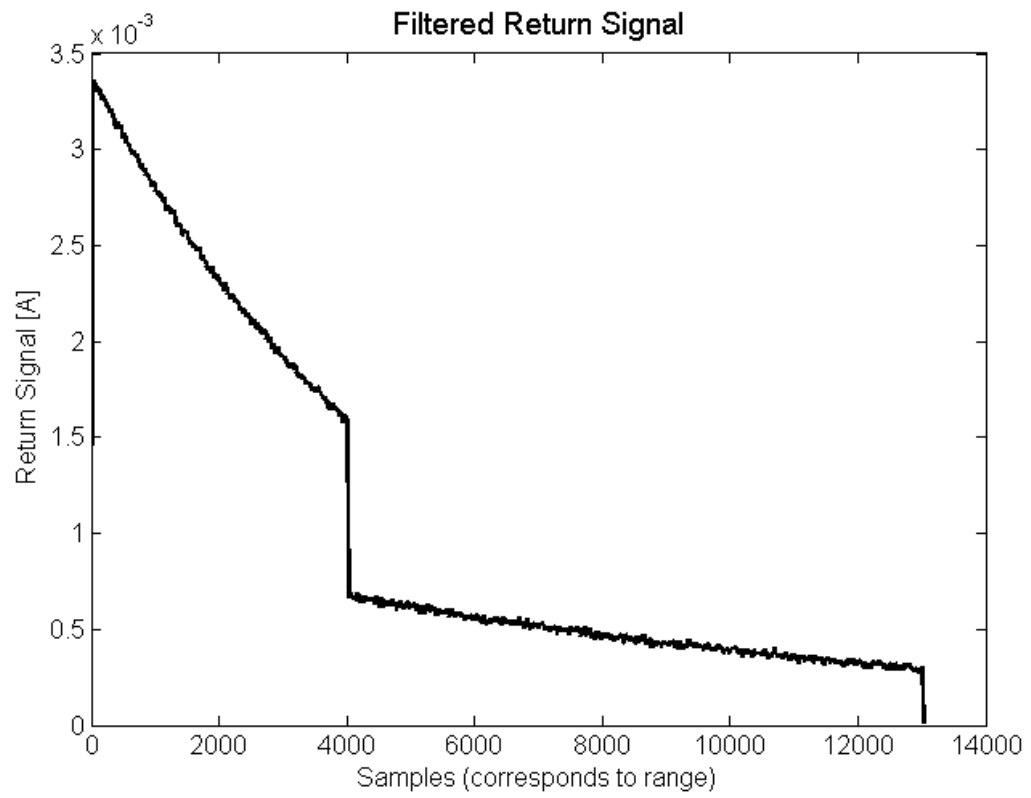


Figure 47: The result of applying a thirty-point averaging filter to the modeled data shown in figure 46

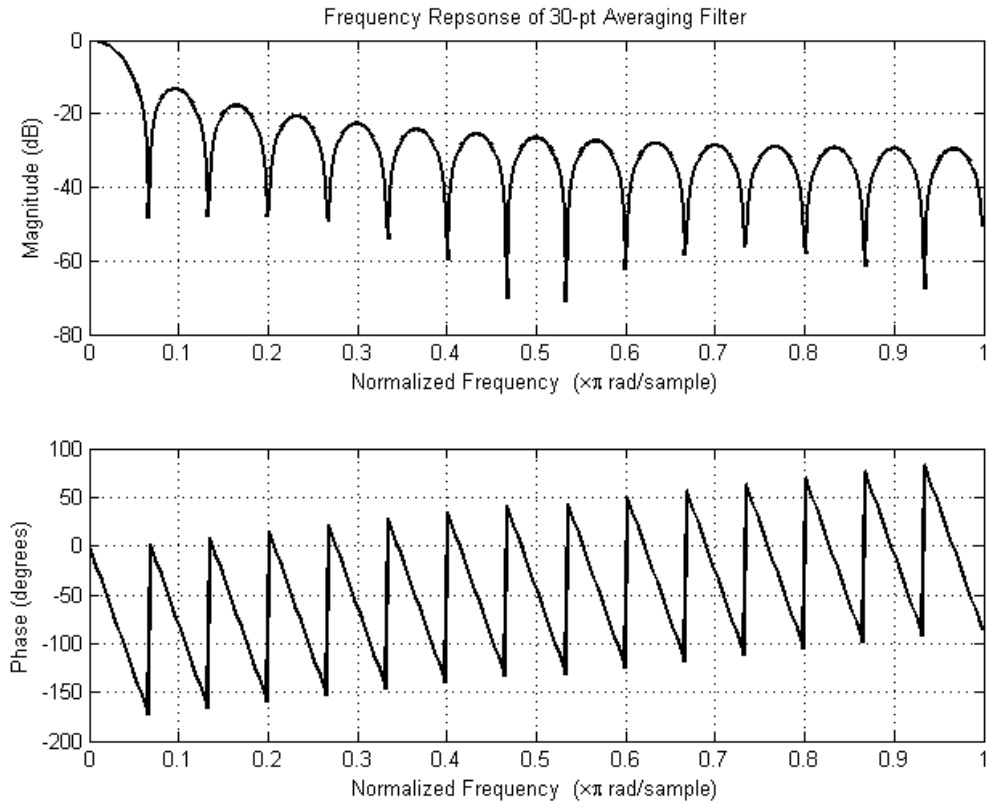


Figure 48: The frequency response of a thirty-point averaging filter.

averaged together resulting in a small ($1 - 5\%$) contribution to S_A retrieval error. This contribution can be calculated using equations 7 and 8 to determine the impact of the K -value error on the return signals, and by using the plot shown in figure 42 to determine the effect this return signal error will have on retrieved S_A . Differences between modeled and actual temperature and pressure are time varying, and difficult to quantify.

Quantization Error

In addition to the noise added to the signal by the detectors themselves, quantization noise is added to both the transmitted and reflected signals when they are digitized so that they can be stored and analyzed via computer. The digitization process consists of sampling the continuous voltage signal produced by the PMTs at discrete time intervals, and rounding the voltage value of each sample to a discrete level that can be represented by the arbitrary number of bits used by the analog to digital (A/D) converter. The difference between the actual voltage value of the input signal from the lidar instrument and the discrete value assigned by the A/D card is the quantization noise (see figure 49). Because the signals from the PMTs in the HSRL instrument are usually within the range of the A/D converter and the quantization levels of the A/D card are uniform, the quantization noise is essentially uniformly distributed random (white) noise. The quantization process can therefore be modeled (in terms of the signal to noise ratio of the overall system) as adding uniformly distributed random noise to each sample as shown in figure 50. The signal to noise ratio associated with the quantization process can be modeled as [35]

$$SNR_Q = \frac{12 \cdot 2^{2b} \sigma_x^2}{X_m^2}, \quad (29)$$

where SNR_Q is the signal to noise ratio resulting from the quantization process, $b+1$ is the number of bits used to represent the quantized data, σ_x^2 is the variance of the signal being quantized and X_m is the range of the quantizer input. The signal to noise ratio associated with the quantization process is on the order of 10^{20} . This means that the noise introduced by the digitization process is insignificant when compared to the noise introduced by the optical detectors.

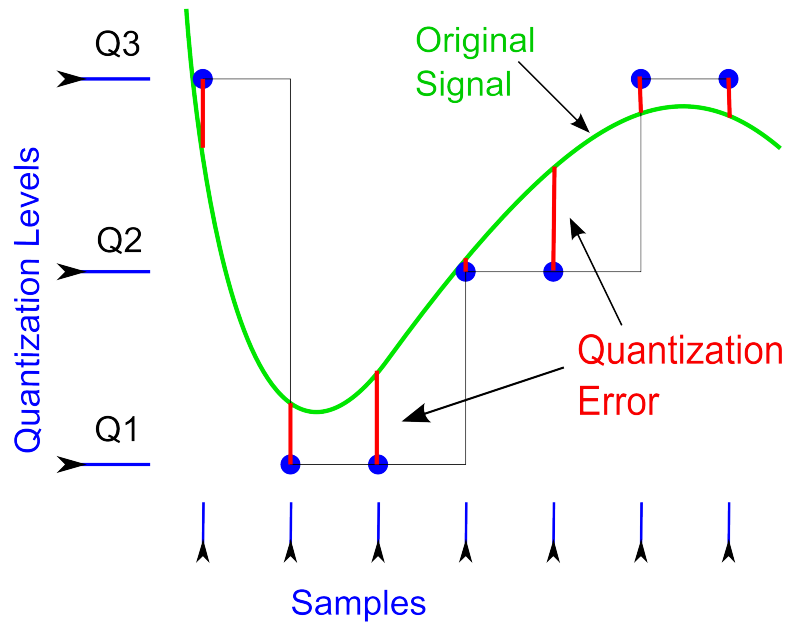


Figure 49: Quantization error is the difference between the actual signal and its quantized value; quantization occurs when the signal is digitized using an A/D converter. In this figure, the red vertical lines represent the quantization error, the blue horizontal lines along the left side mark the quantization levels and the blue vertical lines along the bottom mark the sample points where the original signal (the green line) is sampled and subsequently quantized.

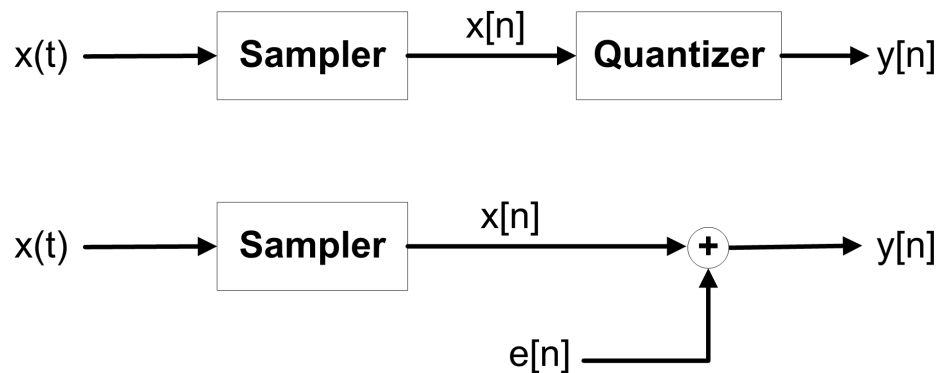


Figure 50: Quantization can be modeled as adding the error term $e[n]$ to the sampled signal, where $e[n]$ is uniformly distributed random noise.

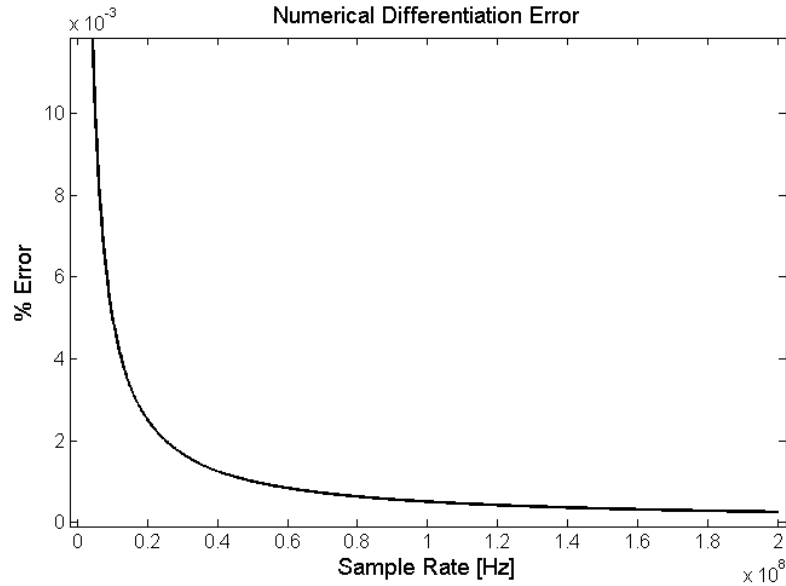


Figure 51: Percent error resulting from using numerical differentiation in the data analysis software. Note that at 200 MHz (the sample rate of the two-wavelength lidar instrument), the error is approximately $2.5 \times 10^{-4}\%$.

Numerical Differentiation Error

The final source of error addressed in this thesis is caused by the use of numerical differentiation to approximate a continuous derivative used to retrieve aerosol optical properties from the raw lidar data. Analysis of differentiation error was carried out empirically by varying the sample rate of modeled lidar returns and observing changes in the results of the data analysis calculations. Numerical differentiation error was determined as percent error from the true value of the calculation results as a function of sample rate, and is plotted in figure 51. The numerical differentiation error for a sample rate of 200 MHz (the sample rate of the HSRL instrument) was calculated to be approximately $2.5 \times 10^{-4}\%$. Considering that the overall error level (at the retrieval output) due to other factors is on the order of 10 – 15%, this error does not significantly affect the outcome of the aerosol property retrieval routine.

Error Impact Summary

The error introduced by the PMTs and through the cavity characterization process is enough to significantly effect the aerosol optical property retrieval results, while error introduced through digitization and the utilization of digital processing techniques is insignificant by comparison. By filtering the data in the temporal and spacial domains, the error is mitigated to the point that aerosol extinction to backscatter ratio can be retrieved within 10 – 15%.

CONCLUDING REMARKS

A HSRL instrument has been developed based on a CFP spectral filter. The CFP spectral filter has the potential benefits of allowing the HSRL technique to be employed over the uv-vis-IR spectral region and is less susceptible to angular misalignment than a flat plate Fabry-Perot spectral filter. A novel robust locking scheme has been developed and employed in the HSRL that allows the CFP to remain resonant with the 532 nm frequency doubled output of the HSRL laser transmitter based on a modulation technique using the 1064 nm cw injection seed laser. Data presented from initial testing of the HSRL indicate that the instrument is capable of measurements at low aerosol optical depths (~ 0.05 at 532 nm), yielding for such low optical depths, lidar ratios consistent with those retrieved from measurements made with a collocated solar radiometer as a part of AERONET (both for the observations reported here and from previous observations at Bozeman) [29, 31]. Additional measurements were made which were consistent with previous multi-instrument aerosol studies at the same geographic location. These comparisons and a model-based error analysis show that SA can be retrieved from the HSRL data with a reasonably high degree of accuracy (within approximately 10%). 532 nm was chosen for the wavelength of the instrument presented in this instrument for the purpose of demonstrating the capabilities of a CFP based HSRL while taking advantage of available hardware. The primary future use of the CFP is intended to be for wavelengths for which there are no readily available absorption filters (such as iodine for 532 nm). The successful operation of the CFP based HSRL instrument indicates that future multi-wavelength CFP-based instruments are feasible.

The HSRL instrument presented in this dissertation represents a meaningful contribution to the fields of science and engineering. The use of a CFP interferometer in

an HSRL instrument is novel, and the CFP has several key advantages over previously used filtering techniques. Unlike gas absorption cells, the CFP interferometer is portable to arbitrary wavelengths. The CFP is much less sensitive to alignment errors and vibrations than previously used flat-plate interferometers. The CFP is much better suited to use in potential future space-based instruments than either gas cells or flat-plate interferometers. The frequency locking technique presented in this dissertation is also novel and represents a contribution to the fields of science and engineering. The development of HSRL technology in general is important to the field of climate and atmospheric science. The atmospheric-aerosol optical properties retrieved using the instrument presented in this paper and other HSRL instruments can be used to better model and understand global climate and temperature.

REFERENCES CITED

- [1] P. Forster, V. Ramaswamy, P. Artaxo, T. Berntsen, R. Betts, D. Fahey, J. Haywood, J. Lean, D. Lowe, G. Mhhre, J. Nganga, R. Prinn, G. Raga, M. Schulz, and R. V. Dorland, “changes in atmospheric constituents and in radiative forcing.’ in: *Climate change 2007: The physical science basis. contributions of working group i to the fourth assessment report of the intergovernmental panel on climate change* [s. solomon and d. qin and m. manning and z. chen and m. marquis and k.b. averyt and m. tignor and and h.l. miller and eds.],” Cambridge University Press, Cambridge, United Kingdom and New York, NY, USA, 2007.
- [2] K. P. Shine, M. Piers, and F. Forste, “The effect of human activity on radiative forcing of climate change: a review of recent development,” *Global and Planetary Change*, no. 20, pp. 205–225, 1999.
- [3] J. Haywood and O. Boucher, “Estimates of the direct and indirect radiative forcing due to tropospheric aerosols: A review,” *Reviews of Geophysics*, vol. 38, no. 4, pp. 513–543, 2000.
- [4] H. Y. Yu, J. Kaufman, M. Chin, G. Feingold, L. A. Remer, T. I. Anderson, Y. Balkanski, N. Bellouin, O. Boucher, S. Christopher, P. deCola, D. Koch, N. Loeb, M. S. Reddy, M. Schulz, T. Takamura, and M. Zhou, “A review of measurement-based assessments of the aerosol direct radiative effect and forcing,” *Reviews of Geophysics*, vol. 6, pp. 613–666, 2006.
- [5] N. Bellouin, J. Haywood, and M. S. Reddy, “Global estimate of aerosol direct radiative forcing from satellite measurements,” *Nature, Letters*, vol. 438, pp. 1138–1141, 2005.
- [6] S. Twomey, “The influence of pollution on the shortwave albedo of clouds,” *J. Atmos. Sci.*, vol. 34, pp. 1149–1152, 1977.
- [7] R. Zhang, G. Li, J. Fan, D. L. Wu, and M. J. Molina, “Intensification of pacific storm track linked to asian pollution.” *Proc Natl Acad Sci USA*, vol. 104, pp. 5295–5299, 2007.
- [8] J. Penner, M. Andreae, H. Annegarn, L. Barrie, J. Feichter, D. Hegg, A. Jayaraman, R. Leaitch, D. Murphy, J. Nganga, and G. Pitari, “Aerosols, their direct and indirect effects, climate change 2001: The scientific basis. contribution of working group i to the third assessment report of the intergovernmental panel on climate change [houghton, j.t., y. ding, d.j. griggs, m. noguer, p.j. van der linden, x. dai, k. maskell, and c.a. johnson (eds.)],” Cambridge University Press, Cambridge, United Kingdom and New York, NY, USA, 2001.

- [9] C. Eichel, M. Kramer, L. Shultz, and S. Wurzler, “The water soluble fraction of atmospheric aerosol particles and its influence on cloud microphysics,” *J. Geophys. Res.*, vol. 101, no. 29, pp. 499–510, 1996.
- [10] V. A. Kovalev and W. E. Eichinger, *Elastic Lidar: Theory, Practice and Analysis Methods*. John Wiley and Sons, New York, 2004, p. 444.
- [11] E. Eloranta, “High spectral resolution lidar,” in *Lidar: Range-resolved remote sensing of the atmosphere (Claus Weitkamp, 2005)*. New York: Springer, pp. 143–163.
- [12] J. D. Klett, “Stable analytical inversion solution for processing lidar returns,” *Appl. Opt.*, vol. 20, pp. 211–220, 1981.
- [13] F. G. Fernald, B. M. Herman, and J. A. Reagan, “Determination of aerosol height distributions by lidar,” *Journal of Applied meteorology*, vol. 77, pp. 433–448, 1989.
- [14] J. W. Hair, C. A. Hostetler, A. L. Cook, D. B. Harper, R. A. Ferrare, T. L. Mack, W. Welch, L. R. Izquierdo, and F. E. Hovis, “Airborne high spectral resolution lidar for profiling aerosol optical properties,” *Appl. Opt.*, vol. 47, pp. 6734–6753, 2008.
- [15] J. Sroga, E. Eloranta, S. Shipley, F. Roesler, and P. Tryon, “High spectral resolution lidar to measure optical scattering properties of atmospheric aerosols. 2: Calibration and data analysis,” *Appl. Opt.*, vol. 22, pp. 3725–3732, 1983.
- [16] S. Shipley, D. Tracy, E. Eloranta, J. Trauger, J. Sroga, F. Roesler, and J. Weinman, “High spectral resolution lidar to measure optical scattering properties of atmospheric aerosols. 1: Theory and instrumentation,” *Appl. Opt.*, vol. 22, pp. 3716–3724, 1983.
- [17] J. W. Hair, L. M. Caldwell, D. A. Krueger, and C.-Y. She, “High spectral resolution lidar with iodine vapor filters: measurement of atmospheric state and aerosol profiles,” *Applied Optics*, vol. 40, pp. 5280–5295, 2001.
- [18] M. Esselborn, M. Wirth, A. Fix, M. Tesche, and G. Ehret, “Airborne high spectral resolution lidar for measuring aerosol extinction and backscatter coefficients,” *Applied Optics*, vol. 47, pp. 346–358, 2008.
- [19] R. J. A. II, L. M. Caldwell, Y. H. Li, D. A. Kreuger, and C. Y. She, “High-spectral resolution lidar measurement of tropospheric backscatter ratio using barium atomic blocking filters,” *Journal of Atmospheric and Ocean Technology*, vol. 7, pp. 876–881, 1990.

- [20] M. Hercher, “The spherical mirror fabry-perot interferometer,” *Applied Optics*, vol. 7, 1968.
- [21] J. R. Johnson, “A high resolution scanning confocal interferometer,” *Applied Optics*, vol. 7, 1968.
- [22] —, “Alignment requirements for mode matching in a confocal fabry-perot interferometer,” *Applied Optics*, vol. 9, 1970.
- [23] G. D. Boyd and J. P. Gordon, “Confocal multimode resonator for millimeter through optical wavelength masers,” *Bell Systems Technology Journal*, no. 40, 1961.
- [24] T. Nishizawa, N. Sugimoto, and I. Matsui, “Development of a dual-wavelength high-spectral-resolution lidar,” *Proc. of SPIE*, vol. 7860, 2010.
- [25] D. Hoffman, K. Repasky, J. Carlsten, and J. Reagan, “Development of a high spectral resolution lidar based on confocal fabry-perot spectral filters,” *Applied Optics*, p. manuscript accepted for publication, 2012.
- [26] A. E. Siegman, *Lasers*. University Science Books, 1986.
- [27] C. R. Mummerlyn and J. W. Balliett, “Alignment requirements for mode matching in a confocal fabry-perot interferometer,” *Applied Optics*, no. 9, 1970.
- [28] K. A. Neal, *A confocal Fabry-Perot Interferometer for Use in Lidar Receivers*. MS Thesis, Montana State University, Bozeman, 2009.
- [29] A. R. Nehrir, K. S. Repasky, J. A. Reagan, and J. L. Carlsten, “Optical characterization of continental and biomass burning aerosols over bozeman montana: A case study of the aerosol direct effect,” *Journal of Geophysical Research*, vol. 116, 2011.
- [30] C. Cattrall, J. Reagan, K. Thome, and O. Dubovik, “Variability of aerosol and spectral lidar and backscatter and extinction ratios for key aerosol types derived from selected aerosol robotic network locations,” *Journal of Geophysical Research*, vol. 110, 2005.
- [31] K. Repasky, J. Reagan, A. Nehrir, D. Hoffman, M. Thomas, J. Carlsten, J. Shaw, and G. Shaw, “Observational studies of aerosols over bozeman, montana, using a two-color lidar, a water vapor dial, a solar radiometer and a ground-based nephelometer over a 24-hour period,” *Journal of Atmospheric and Ocean Technology*, vol. 28, pp. 320–336, 2010.
- [32] J. E. Yorks, D. L. Hlavka, W. D. Hart, and M. J. McGill, “Statistics of cloud optical properties from airborne lidar measurements,” *Journal of Atmospheric and Ocean Technology*, vol. 28, no. 7, p. 869883, 2011.

- [33] W.-N. Chen, C.-W. Chiang, and J.-B. Nee, "Lidar ratio and depolarization ratio for cirrus clouds," *Journal of Applied Optics*, vol. 41, no. 30, p. 64706476, 2002.
- [34] H. Corp., *High Speed Gated PMT Module H7680, H7680-01 Instruction Manual*. Hamamatsu Electron Tube Center, Japan, 2005.
- [35] A. V. Oppenheim, R. W. Shafer, and J. R. Buck, *Discrete Time Signal Processing*. Prentice Hall, Upper Saddle River, NJ, 1999, pp. 194–197.

APPENDIX A

MATLAB CODE

S_ARetrievalProgram

```

%constants , etc:
start = 1;
lth = length(trans1); %return length in samples
step = 100;
n = [start:step:lth];
n = 1000;
h = (n/200000000)*((3*(10^8))/2); %range bins
%h = (n/100000000)*((3*(10^8))/2);
T = 270.15 - (.010045.*h); % .010045 or .006545 %temperature model
p = ((270.15./T).^(-.034164/.010045)).*(1.013e5); %pressure model
lamda = .000000532; %wavelength [m]
m = (14.1/1000)/(6.02*10^23);
c = 3*10^8;
k = 1.3806503*10^(-23);
sigma0 = (2*pi)/lamda;
n = 0;
step2 = .01;
s = zeros(ceil((2*.0003e6)/step2),1);
%Doppler broadening fxn:
spread = zeros(ceil((2*.0003e6)/step2),ceil(lth/step));
for sigma = sigma0-.0003e6:step2:sigma0+.0003e6-step2 %0.00236
    n = n +1;
    s(n) = sigma;
    spread(n,:) = sqrt((m*(c^2))./(8.*pi.*(sigma0^2).*k.*T)).* ...
        ... exp(-(m*(c^2))./(8.*pi.*(sigma0^2).*k.*T).*((sigma-sigma0)^2));
end
l = (2*pi)./s;
f = (3e8)./l;
df = ((3e8)/.000000532)-f;
df = df./(1e9);

%cavity

lamda_o = 532e-9;
lamda = 1:.000000002:1.00008;
lamda = lamda .* lamda_o;
absorption = .01;
freq = (3e8)./lamda;

for n = 1:l
    R = .86;
    F = (4*R)/((1-(R))^2);
    lth = .01;
    T = (.5)/(1+(F*(sin((4*pi*lth)./lamda)).^2));
    R = (1-(T.*.3)).*.7;
end

%laser

```

```

laser = exp(-(((df-0).^2)./(2*((1/23.5482)^2))));

%calculations:

R = [zeros(1,10249) R zeros(1,9750)];
T = [zeros(1,10249) T zeros(1,9750)] ./ 3;

%cavity transmission parameters:

Kaa = sum(T'.*laser.*((df(4)-df(5))*(1e8)).*30000);
Kma = sum(T'.*spread(:,5).*((df(4)-df(5))*(1e8)).*12000);
Kmm = sum(R'.*spread(:,5).*((df(4)-df(5))*(1e8)).*180);
Kam = sum(R'.*laser.*((df(4)-df(5))*(1e8)).*4400);

m = 1:1:size(trans1,2);
range = (m/200000000)*((3*(10^8))/2);
pa = trans1.*-1;
pm = reflected1.*-1;
gamma = .1;

%separating molecular and aerosol returns:

Pa0 = ((pa./gamma)-((Kma.*pm)./(gamma.*Kmm)))./(Kaa-((Kam.*Kma)/Kmm));
Pm0 = ((pm./gamma)-((Kam.*pa)./(gamma.*Kaa)))./(Kmm-((Kma.*Kam)/Kaa));

%molecular scattering profile:

h = range;
T = 293.15 - (.010545.*h);
p = ((293.15./T).^(-.034164/.006545)).*(1.013e5).*85;

wav = 532;
backscatter_M = (374.28*(p./T)./(wav^4));

sigma_M = ((backscatter_M.*(8*pi))./3);

S_M = (8*pi)/3;

B_ratio = Pa0./Pm0;
B_ratio(find(Pm0 == 0))=2;
backscatter_A = B_ratio.*(ones(size(B_ratio,1),1)*backscatter_M);
trans = log(Pa0./backscatter_A);
delr = range(5)-range(4);
pm_model = Pm0;

for n = 1:size(range,2)
    pm_model(:,n) = backscatter_M(n)*exp(-2*sum(alpha_M(1:n)).*delr);
    Tm(n) = exp(-2*sum(sigma_M(1:n)).*delr); %modeled molecular trans
end

%SA retrieval:

```

```
T2 = Pm0./backscatter_M; %transmission (2-way)
Ta2 = T2 ./ Tm; %aerosol transmission
AOT2 = -.5.*(log(Ta2)); %AOT
%now differentiate AOT2 with respect to r:
sigma_A = pa_model .* 0;
for n = 2:size(pa_model,2)
    sigma_A(n) = 2.*(AOT2(n)- AOT2(n-1))/delr; %aerosol extinction
end

S = sigma_A./backscatter_A; %aerosol extinction to backscatter ratio
```